Regulatory myeloid cells paralyze T cells through cell-cell transfer of the metabolite methylglyoxal

Tobias Baumann[1], Andreas Dunkel[2], Christian Schmid[3], Sabine Schmitt[4], Michael Hiltensperger[5], Kerstin Lohr[1], Viktor Laketa[6], Sainitin Donakonda[1], Uwe Ahting[7], Bettina Lorenz-Depiereux[8], Jan E. Heil[9], Johann Schredelseker[10], Luca Simeoni[11], Andreas Fecher[12], Nina Körber[13], Tanja Bauer[13], Norbert Hüser[14], Daniel Hartmann[14], Melanie Laschinger[14], Kilian Eyerich[15], Stefanie Eyerich[16], Martina Anton[1], Matthew Streeter[17], Tina Wang[18], Burkhard Schraven[11], David Spiegel[17,19], Farhah Assaad[20], Thomas Misgeld[12], Hans Zischka[4,21], Peter J. Murray[22], Annkristin Heine[23,24], Mathias Heikenwälder[25], Thomas Korn[5], Corinna Dawid[3], Thomas Hofmann[2,3], Percy A. Knolle[1,26,27]*† & Bastian Höchst[26]*†

Affiliations:

[1]Institute of Molecular Immunology & Experimental Oncology, Klinikum rechts der Isar, School of Medicine, Technical University of Munich (TUM), Germany
[2]Leibniz-Institute of Food Systems Biology at the TUM, Germany
[3]Chair of Food Chemistry and Molecular Sensory Science, TUM, Germany
[4]Institute for Toxicology and Environmental Hygiene, School of Medicine, TUM, Germany
[5]Department of Experimental Neuroimmunology, Klinikum rechts der Isar, School of Medicine, TUM, Munich, Germany.
[6]Department of Infectious Diseases, German Center for Infection Research (DZIF), University Heidelberg, Germany
[7]Institute of Human Genetics, Stoffwechsel-Zentrum, Klinikum rechts der Isar, School of Medicine, TUM, Germany
[8]Institute of Human Genetics, Helmholtz Zentrum München, Munich, Germany
[9]Carl Zeiss Microscopy GmbH, Göttingen, Germany
[10]Walther Straub Institute of Pharmacology and Toxicology, Faculty of Medicine, Ludwig-Maximilians-Universität München, Munich, Germany
[11]Institute of Molecular and Clinical Immunology, Otto-von-Guericke University, Magdeburg, Germany
[12]Institute of Neuronal Cell Biology, TUM, Munich Cluster for Systems Neurology and German Center for Neurodegenerative Diseases, Munich, Germany
[13]Institute of Virology, Helmholtz Zentrum München, Munich, Germany
[14]Department of Surgery, Klinikum rechts der Isar, School of Medicine, TUM, Germany
[15]Department of Dermatology and Allergy, TUM, Germany
[16]ZAUM-Center of Allergy and Environment, TUM and Helmholtz Center Munich
[17]Department of Chemistry, Yale University, New Haven, USA
[18]Broad Institute of Harvard & MIT, Cambridge, USA
[19]Department of Pharmacology, Yale University, New Haven, USA
[20]Botany, Plant Science Department, Centre for Life Science, TUM, Germany
[21]Institute of Molecular Toxicology and Pharmacology, Helmholtz Center Munich, Neuherberg, Germany.
[22]Max-Planck Institute for Biochemistry, Martinsried, Germany
[23]Medical Clinic III for Oncology, Hematology and Rheumatology, University Hospital Bonn, Germany
[24]Institute of Experimental Immunology, University Bonn, Germany
[25]Division of Chronic Inflammation and Cancer, German Cancer Research Center (DKFZ), Heidelberg, Germany
[26]Institute of Molecular Immunology, School of Life Sciences, TUM, Munich, Germany
[27]German Center for Infection Research, Munich Site, Germany
*,† these authors contributed equally and serve as corresponding authors

Address for correspondence
Bastian Höchst, PhD
Institute of Molecular Immunology, TUM School of Life Science, Weihenstephan, Alte Akademie 8, 85354 Freising, Germany
& Percy A. Knolle, MD
Institute of Molecular Immunology and Experimental Oncology, TUM School of Medicine, Ismaningerstr 22, 81675 München, Germany, and TUM School of Life Science, Weihenstephan, Alte Akademie 8, 85354 Freising, Germany
Tel: +49 89 4140 6920
e-mail: Bastian.Hoechst@tum.de & Percy.Knolle@tum.de

Abstract

Regulatory myeloid immune cells, such as myeloid-derived suppressor cells (MDSCs), populate inflamed or cancer tissue and block immune cell effector functions. Lack of mechanistic insight into MDSC suppressive activity and a marker for their identification hampered attempts to overcome T cell-inhibition and unleash anti-cancer immunity. Here we report that human MDSCs were characterized by strongly reduced metabolism and conferred this compromised metabolic state to $CD8^+$ T cells thereby paralyzing their effector functions. We identified accumulation of the dicarbonyl-radical methylglyoxal, generated by semicarbazide-sensitive amine oxidase (SSAO), to cause the metabolic phenotype of MDSCs and MDSC-mediated paralysis of $CD8^+$ T cells. In a murine cancer model, neutralization of dicarbonyl-activity overcame MDSC-mediated T cell-suppression and together with checkpoint inhibition improved efficacy of cancer immune therapy. Our results identify the dicarbonyl methylglyoxal as marker metabolite for MDSCs that mediates T cell paralysis and can serve as target to improve cancer immune therapy.

Introduction

Immune surveillance against infection and cancer relies on the appropriate induction of immune cell effector functions in peripheral tissues[1]. The mechanisms determining activation of innate immune cells such as monocytes or macrophages through immune sensory receptors or cytokines, and of adaptive immune cells such as T cells through the cell receptor and costimulatory signals have been well characterized[2]. However, regulatory or inhibitory mechanisms that control immune cell function, in particular $CD8^+$ T cell effector functions are increasingly recognized as key determinants for the outcome of immune responses in peripheral tissues[3, 4]. The discovery of co-inhibitory molecules on T cells such as programmed cell death protein 1 (PD-1) as checkpoints of immunity has opened new avenues for targeted immune intervention to reconstitute tumor-specific T cell immunity in several cancer entities[5]. Furthermore, regulatory immune cell populations responsible for such control of T cell effector functions and their suppressive mechanisms have been intensively studied. Identification of Foxp3 as key transcription factor determining induction of regulatory $CD4^+$ T (T_{reg}) cells[6] paved the way to elucidate the molecular mode-of-action as to how these T_{reg} cells controlled effector $CD8^+$ T cell functions[7], which led to development of targeted immune strategies to improve anti-cancer T cell immunity in preclinical model systems and patients[8, 9, 10]. Besides T_{reg} cells, also regulatory myeloid cells were described, termed myeloid-derived-suppressor-cells (MDSCs)[11], -that can be of monocytic (M-MDSCs) or polymorph nuclear (PMN-MDSCs) origin. Whereas during acute inflammation monocytes, macrophages and granulocytes are found at sites of inflammation and locally enhance T cell immunity, such as monocytes promoting local T cell proliferation and immunity during acute liver inflammation[12], MDSCs typically arise in situations of chronic inflammation in peripheral tissues including cancer[13, 14, 15, 16]. Since discriminative molecular markers for unequivocal identification of MDSCs do not yet exist, the molecular mechanisms controlling T cell effector functions have been difficult to study. Here, we report on the identification of a marker metabolite that identifies MDSCs and is causally involved in metabolic suppression of T cell effector function.

Results

Dormant metabolic phenotype in MDSCs

Suppressive myeloid cells arise during chronic inflammation in tissues[17], and tissue stromal cells induce transition of monocytes into monocytic MDSCs[16]. We exploited this capacity of stromal cells to convert human peripheral blood monocytes into MDSCs, which are phenotypically similar to $CD14^{+}HLA\text{-}DR^{-/low}$ suppressive myeloid cells directly isolated from cancer patients[16], to characterize the mechanism of MDSC-mediated T cell suppression. Transcriptome analysis showed less than 200 differentially expressed genes between MDSCs and monocytes, which did not include surface molecules suitable for phenotypic discrimination or known immune suppressive mediators to explain their suppressive activity (**supplementary table I-IV, Extended Data Fig. 1**). Consistently, blockade of known immune suppressive mediators did not prevent MDSC-mediated T cell suppression (**Extended Data Fig. 2**). Surprisingly, we found downregulation of genes encoding glycolysis-related enzymes in MDSCs (**Fig. 1a, and Extended Data Table V**). Indeed, MDSCs showed reduced glucose uptake and Glut1 surface expression (**Fig. 1b**), the main transporter mediating glucose uptake in immune cells. As predicted from gene expression analysis, hexokinase activity was lower in MDSCs (**Fig. 1c**). To validate these results, we isolated $CD14^{+}HLA\text{-}DR^{-/lo}$ cells from tumor tissue of patients with hepatocellular carcinoma by enzymatic digestion followed by density centrifugation and flow cytometric cell sorting. We confirmed reduced glucose uptake and hexokinase activity in $CD14^{+}HLA\text{-}DR^{-/low}$ cells isolated from tumor tissue of cancer patients (**Fig. 1d,e, and Extended Data Table VI**), which are considered to represent MDSCs. Strikingly, MDSCs failed to utilize glucose for glycolysis and also showed reduced cellular bioenergetics, i.e. lower mitochondrial membrane potential quantified by the potentiometric mitochondrial dye $DilC_1(5)$ and lower baseline mitochondrial respiration revealed by extracellular flux analysis (**Fig. 1f-h**). Together with reduced cellular ATP content (**Fig. 1i**) these results revealed a rigorous reduction of cell metabolism to very low levels in viable MDSCs, and raised the question as to whether this metabolic dormancy was involved in suppression of T cells.

MDSCs paralyze CD8 T cell function

Signaling processes downstream of the TCR and the costimulatory receptor CD28 are important for induction of glycolysis and glycolytic enzymes[18, 19]. In particular hexokinase can also act as protein kinase enhancing T cell activation[20]. After contact with MDSCs, activation-induced phosphorylation of key protein kinases downstream of the TCR was almost completely prevented (**Fig. 2a** and **supplementary Fig. 3a-d**), indicating suppression of TCR signaling after contact with MDSCs as compared to monocytes. T cell antigen receptor (TCR) and CD28 signaling in $CD8^+$ T cells act synergistically to increase glucose uptake and glycolysis[21], which supports execution of T cell effector function[22]. Co-culture of anti-CD3/28-activated $CD8^+$ T cells with MDSCs for 30 min fundamentally changed their metabolism. Such MDSC-exposed T cells failed to increase glucose uptake, Glut-1 surface expression and hexokinase activity after activation, and were similar to non-activated T cells (**Fig. 2b,c** and **Extended Data Fig. 4a-c**). In contrast, contact with monocytes led to further increased glucose uptake and Glut-1 surface expression by activated T cells (**Fig. 2b, c** and **Extended Data Fig. 4a-c**). Impaired glucose uptake into syngeneic $CD8^+$ T cells was also observed after co-culture with tumor-infiltrating $CD14^+HLA\text{-}DR^{-/lo}$ cells from cancer patients (**Fig. 2d**), confirming the similarity between stromal cell-induced MDSCs and MDSCs from cancer tissue. Furthermore, glycolysis and mitochondrial respiration were not upregulated in T cells activated in presence of MDSCs as compared to monocytes (**Fig. 2e, f** and **Extended Data Fig. 4d, e**). In consequence, ATP concentrations were reduced in T cells activated in presence of MDSCs (**Fig. 2g** and **Extended Data Fig. 4f**). Strikingly, contact with MDSCs also completely prevented cytokine expression (tumor necrosis factor (TNF) and interleukin-γ (IFN-γ)) and granzyme B release in T cells, and curtailed activation-induced proliferation of $CD45RA^+CD62L^{hi}$ naïve, $CD45RA^+CX_3CR1^+$ effector, $CD45RO^+CD62L^+$ central memory or $CD45RO^+CX_3CR1^+$ effector memory $CD8^+$ T cells (**Fig. 2h, Extended Data Fig. 5a-g**). Importantly, when activated $CD8^+$ T cells were physically separated by transwell, MDSCs did not exert their suppressive activity any more (**Fig. 2i**). These results suggested that MDSCs prevented T cell activation by inhibiting signaling processes in a cell-contact dependent fashion, which consecutively caused failure to upregulate metabolism and effector function.

These results led us to study MDSCs - T cell interaction further. We stained MDSCs or monocytes with dyes that labeled mitochondria, endoplasmic reticulum, cytosolic proteins or plasma membranes. We detected transfer of cytosolic constituents, either parts of labeled cellular organelles or remaining cytosolic dye, into $CD8^+$ T cells when located in direct vicinity (**Fig. 3a-c**, **Extended Data Movies 1, 2**). Also labeled cytosolic constituents from tumor-infiltrating MDSCs were transferred to T cells (**Fig. 3d**). In contrast, no or very little transfer of cytosolic constituents was observed from human keratinocytes or fibroblasts to $CD8^+$ T cells (**Fig. 3e**), consistent with restriction of such transfer between immune cells[23, 24]. Of note, also $CD4^+$ T cells and natural killer T (NKT) cells received cytosolic constituents from MDSCs (**Extended Data Fig. 6a**). No transfer of surface molecules, however, was observed between MDSCs and T cells (**Fig. 3f**). To demonstrate that such cell-cell transfer also occurred *in vivo*, we transferred mouse $CD45.1^+$ OT-I $CD8^+$ T cells into tumor-bearing transgenic mice where myeloid cells expressed green fluorescent protein (GFP) targeted to the mitochondrial matrix (*LysM-Cre x Rosa26-mitoGFP*). Transferred $CD8^+$ T cells, which were re-isolated from tumor tissue, were GFP^{pos} indicating cytosolic transfer from myeloid to $CD8^+$ T cells (**Extended Data Fig. 6c**). $GFP^{pos}CD45.1^+CD8^+$ T cells isolated from the spleen, however, showed normal proliferation, whereas $GFP^{pos}CD45.1^+CD8^+$ T cells from tumor tissue showed no proliferation after activation (**Extended Data Fig. 6d**), indicating that transfer of GFP in different anatomic compartments by presumably different cells has a different effect on T cell function – similar to the opposite effects of monocytes and MDSCs *in vitro* on the function of T cells in their direct vicinity. We excluded transfer of entire organelles containing mitochondrial DNA, because donor-specific single-nucleotide-polymorphisms in mitochondrial DNA from MDSCs were not detected in acceptor $CD8^+$ T cells (**Fig. 3g**). Together, these results revealed transfer of cytosolic constituents rather than entire organelles from MDSCs into T cells in a cell-contact dependent fashion.

MDSCs paralyze CD8 T cells through the dicarbonyl methylglyoxal

Given the importance of glycolysis for immune cell activation[22, 25, 26], we reasoned that blocking of mitochondrial complex I activity through dimethylbiguanide (DMBG) or rotenone, which increases glycolysis[27, 28, 29, 30], might revert the suppressive phenotype of MDSCs. However, only

DMBG-treatment of MDSCs reversed suppression of T cell proliferation (**Fig. 4a**) and re-installed TCR signaling (data not shown), indicating a function of DMBG distinct from influencing mitochondrial respiration. Guanidines also neutralize dicarbonyls that glycate molecules or proteins with amino groups[31, 32], which led us to search for this class of reactive metabolites in MDSCs. Strikingly, using highly sensitive detection of metabolites by ultrahigh performance liquid chromatography data independent acquisition tandem mass spectrometry (UHLC-TOF-DIA-MS/MS)[33] we identified methylglyoxal, a prototypic α-dicarbonyl[34], to be 30-fold enriched in MDSCs (**Fig. 4b,c**, **supplementary table VII** and **supplementary Fig. 7a**). We confirmed accumulation of methylglyoxal at the level of individual cells using the methylglyoxal-specific fluorescent sensor methyl-diaminobenzene-BODIPY (MBo)[35]. MDSCs showed higher MBo-fluorescence compared with monocytes indicating presence of methylglyoxal (**Fig. 4d**). Importantly, among myeloid $CD14^+$ cells from cancer tissue we found MBo^{hi} cells that were $HLA\text{-}DR^{-/lo}$ (**Fig. 4e**), indicating that also patient-derived MDSCs had accumulated methylglyoxal. Moreover, high MBo-fluorescence was found in both mouse $CD11b^+Ly6C^+$ and $CD11b^+Ly6G^+$ cells isolated from tumor tissue or from the inflamed CNS tissue during the recovery phase of EAE (**Fig. 4f**). Systematic analysis in different human immune cell populations revealed that high MBo-fluorescence was selectively found in MDSCs and could therefore serve as molecular metabolic marker (**Extended Data Fig. 7b**). When isolated from HCC patients MBo-fluorescence was only detected in M-MDSCs but not in PMN-MDSCs (**Fig. 4g**), pointing towards differences between human and murine PMN-MDSCs. Guanidines neutralize glycation activity of dicarbonyls[36, 37]. Strikingly, after incubation with DMBG but not molecules lacking guanidine-groups, human MDSCs lost MBo-fluorescence and regained the capacity to take up glucose (**Fig. 4g,h**, **Extended Data Fig. 7c**). Furthermore, DMBG also augmented aerobic glycolysis and mitochondrial respiration in MDSCs up to the level observed in monocytes (**Fig. 4i,j**). We conclude from these results that methylglyoxal not only serves as metabolic marker for MDSCs but that methylglyoxal glycation activity, which is sensitive to DMBG neutralization, contributed to the dormant metabolic phenotype of MDSCs and led us to characterize why methylglyoxal accumulated in MDSCs.

Methylglyoxal can be generated by three distinct pathways (**Fig. 5a**), as byproduct of glycolysis from glyceraldehyde 3-phosphate and dihydroxyacetone phosphate through spontaneous dephosphorylation[38, 39], from acetol by acetone/actol mono-oxygenase (AMO; cytochrome P4502E1)[40], or from aminoacetone by semicarbazide-sensitive amine oxidase (SSAO)[38, 41]. We performed competitive pulse-chase metabolic labeling experiments (50% $^{13}C_6$-glucose/50% $^{12}C_6$-glucose), to discriminate between these pathways, i.e. methylglyoxal should contain three ^{13}C-atoms when derived from dihydroxyacetone phosphate[38, 39], two ^{13}C-atoms when derived from SSAO-activity and no ^{13}C-atoms when derived from AMO-activity. A regular mass of 206 Da was detected by UHPLC-TOF-DIA-MS/MS for 49% of 3-nitrophenylhydrazine-bound methylglyoxal and 207 Da for 3%, reflecting the natural ^{13}C-isotope distribution (**Fig. 5b**). However, 47% of methylglyoxal detected in MDSCs had a mass of 208 Da (**Fig. 5b**), i.e. containing two ^{13}C-atoms, and indicated that methylglyoxal was generated by SSAO. This was corroborated by increased expression of the *AOC3* gene that codes for SSAO (**Fig. 5c**). Intracellular methylglyoxal abundance is regulated by glyoxalase and by glutathione, which neutralize dicarbonyls[36]. Both, glyoxalase I activity and cellular glutathione content were reduced in MDSCs compared to monocytes (**Fig. 5d,e**), indicating a dysbalance between generation and neutralization of methylglyoxal. SSAO-inhibition with hydralazine or PXS-4618A prevented methylglyoxal accumulation in MDSCs and reconstituted glucose uptake (**Fig. 5f,g**). These results prompted us to examine whether methylglyoxal was involved in T cell suppression by MDSCs.

Within 10 min after contact with MDSCs but not monocytes, we detected methylglyoxal in $CD8^+$ T cells, which was not observed when MDSCs were pretreated with DMBG (**Fig. 6a**). DMBG treatment of MDSCs before co-culture also reconstituted $CD8^+$ T cell uptake of glucose (**Fig. 6a**). Furthermore, activation-induced cytokine production and granzyme B release were fully functional in $CD8^+$ T cells, when MDSCs or $CD8^+$ T cells were pretreated with DMBG (**Fig. 6b, Extended Data Fig. 8a-d**) demonstrating that DMBG abrogated the suppressive effect by acting in MDSCs as well as in $CD8^+$ T cells. In murine PMN-MDSCs, suppression of T cells was also abolished by DMGB (**Extended Data Fig. 8d**). In contrast, DMBG did not show any effect on suppression mediated by regulatory T cells (**Extended Data Fig. 8e**), which were also negative for MBo-fluorescence. After separation from MDSCs, the suppression of T cells lasted for 3-4 h, and

DMBG shortened this time to 1 h until T cells started to take up glucose again (**Extended Data Fig. 8g,h**). In line with these findings, T cells co-cultured with MDSCs regained their capacity to express cytokines upon activation at 4 h after re-isolation and separation from MDSCs (**Fig. 6b**). This recovery phase was again shortened to 1 h by DMBG (**Fig.6b**). MDSC-mediated suppression of T cell proliferation was overcome by DMBG or other guanidine-containing molecules (**Fig. 6c, Extended Data Fig. 8a**). Of note, $CD8^+$ T cell functions, which were augmented by co-culture with monocytes, were not further increased by monocyte pretreatment with DMBG (**Fig. 6c, Extended Data Fig. 8b**). Importantly, we did not observe increased apoptosis in T cells co-cultured with MDSCs (**Extended Data Fig. 8i,j**), indicating that the suppressive activity of MDSCs did not kill but rather stunned T cells.

Importantly, the suppression of T cell proliferation was strongest for MDSCs isolated from liver cancer tissue and weaker when isolated from peritumoral liver tissue or peripheral blood, isolated from the same patients with liver cancer, as shown by titrating numbers of MDSCs (**Fig. 6d**). DMBG reversed the suppressive effect of all M-MDSCs isolated from cancer, peritumoral liver tissue and blood (**Fig. 6d**). Consistent with the lower suppressive capacity, M-MDSCs isolated from blood showed weak to undetectable MBo-fluorescence effect (**see Fig. 4g**). Nevertheless, DMBG-mediated reversal of T cell suppression indicated that methylglyoxal was still present and functional, albeit at low levels was still present – albeit at low levels. It was not possible to isolate PMN-MDSCs from tissue in sufficient quantities for suppression assays, but tumor tissue-derived PMN-MDSCs did not show MBo-fluorescence and PMN-MDSCs isolated from blood of tumor patients did not show suppressive activity (**Extended Data Fig. 8f**), which is in line with findings from other groups [42, 43, 44].

Since methylglyoxal readily reacts with L-arginine, which is required for T cell activation [45, 46], we investigated whether the suppressive effect of MDSCs-transferred methylglyoxal was mediated by depletion of amino acids, in particular L-arginine. To this end, we determined by mass spectrometry the composition of free amino acids as well as advanced glycation end products (AGPs) of amino acids and protein-bound amino acids in T cells. These experiments showed a significant reduction in free L-arginine in T cells after co-culture with MDSCs but not monocytes (**Fig. 6e,f**). Importantly, we also detected a simultaneous increase of the L-arginine-derived

reaction products with methylglyoxal, i.e. AGPs hydroimidazolone (MG-H1) and argpyrimidine (Fig 6e,f). Furthermore, we detected a reduction of L-glutamine (Fig. 6f), which serves as a precursor for glutathione that can scavenge methylglyoxal [34]. There was no reduction in other amino acids or AGPs in MDSC-exposed T cells (Extended Data Fig. 9) demonstrating a selective depletion of amino acids that are critical for T cell activation. In summary, these data show that contact with MDSCs led to depletion of L-arginine and concomitant increase in methylglyoxal-derived glycation products of L-arginine in T cells, which may explain the methylglyoxal-mediated paralysis of their effector functions.

Methylglyoxal neutralization rescues anti-tumor immunity synergizing with checkpoint inhibition

We employed the mechanistic understanding of MDSC-induced suppression of $CD8^+$ T cell effector function to increase efficacy of cancer immune therapy. Mouse melanoma cells expressing ovalbumin (B16-OVA) were s.c. implanted into mice, followed ten days later by therapeutic vaccination against ovalbumin to induce $CD8^+$ T cell immunity against ovalbumin-expressing cancer cells. Separate treatment with therapeutic vaccination, DMBG or checkpoint inhibition with anti-PD-1 alone showed no or only marginal effects on tumor growth. The combination of vaccination with DMBG showed a reduction in tumor growth (Fig. 7a). However, strong and lasting tumor regression was observed when DMBG was combined with anti-PD-1 treatment independently from therapeutic vaccination. After 30 days, however, a relapse of tumor growth was observed. Importantly, we found that tumor cells growing out after combined DMBG/anti-PD-1 treatment had lost ovalbumin expression (Fig. 7a, Extended Data Fig. 10 b). These results clearly demonstrated a synergistic effect of DMBG together with checkpoint inhibition therapy using anti-PD1 to increase cancer-specific immune responses. Most likely, DMBG reversed the suppressive effect of MDSCs on $CD8^+$ T cells specific for immunogenic cancer antigens, locally in tumor tissue, which might have increased the immune pressure on the tumor and selection of tumor cells lacking ovalbumin expression.

These results prompted us to characterize $CD8^+$ T cells and $CD11b^+$ cells from tumor tissue and spleen in detail. At day 17 after tumor inoculation, most $CD11b^+Ly6C^+$ and $Ly6G^+$ cells isolated

from cancer tissue but not spleen showed MBo-fluorescence and were not capable of taking up glucose (**Fig. 7b,c, Extended Data Fig. 10c,d,e**). In mice treated with DMBG, no MBo-fluorescence was detected anymore in these cells and glucose uptake was rescued (**Fig. 7c,d**) independently of vaccination or anti-PD-1 treatment. To directly investigate their suppressive function, we isolated $CD11b^+Ly6C^+$ cells and incubated them *ex vivo* with $CD8^+$ T cells. While $CD11b^+Ly6C^+$ cells from cancer tissue irrespective of vaccination showed potent suppression of activation-induced T cell proliferation, cells isolated from DMBG-treated mice did not suppress $CD8^+$ T cell proliferation anymore, while $CD11b^+Ly6C^+$ cells isolated from spleen always provided similar support for T cell proliferation (**Fig. 7d, Extended Data Fig. 10f,g**). The numbers of effector CX_3CR1^+ $CD8^+$ T cells found in cancer tissue increased after vaccination and were not further augmented by DMBG-treatment, but these cells did not show MBo-fluorescence anymore and took up more glucose *ex vivo* (**Fig. 7e**). Most importantly, numbers of $CD8^+$ T cells isolated from cancer tissue, which responded to antigen-specific restimulation *ex vivo* with robust cytokine expression, only increased when mice received vaccination in combination with DMBG-treatment. While neither MBo-fluorescence nor glucose uptake in monocytic cells in the tumor were influenced by anti-PD-1 treatment alone, after combination with DMBG a significantly increased number of antigen-specific cytokine-producing $CD8^+$ T cells in the tumor was observed (**Fig. 7f-i, Extended Data Fig. 10h,i**). Together, these results indicated that MDSCs paralyzed antigen-specific $CD8^+$ T cells in cancer tissues by a DMBG-sensitive mechanism that was mechanistically distinct from the inhibitory effect through immune checkpoints and might explain the synergistic effect in combination with checkpoint inhibition to increase cancer immune therapy.

Discussion

Here, we identify methylglyoxal as metabolic marker of MDSCs, which is responsible for the dormant metabolic phenotype of MDSCs and for MDSC-mediated immune paralysis of $CD8^+$ T cells, and can serve as therapeutic target in combination with checkpoint inhibition to improve immunotherapy against cancer.

MDSCs primarily inhibit effector functions of T cells and thereby impair immunity against cancer[47]. Many inhibitory mechanisms have been attributed to MDSC-mediated suppression of T

cell effector function, such as IL-10, TGF-β, arginase-1 to deplete extracellular L-arginine, indoleamine 2,3-dioxygenase (IDO) and iNOS[48]. However, the lack of a molecular marker to unequivocally identify MDSCs made it difficult to assign to MDSCs the production of any of the aforementioned regulatory molecules, which are often are also produced by other immune regulatory cell populations like regulatory T cells[7]. MDSCs are believed to be contained among $CD14^{+}HLA\text{-}DR^{-/lo}$ cells[47]. Using high-resolution mass-spectrometry, we have identified methylglyoxal as marker metabolite for MDSCs that is generated from acetyl-CoA and glycine through the enzyme SSAO. Detection with MBo revealed at the single-cell level that methylglyoxal accumulated selectively in $CD14^{+}HLA\text{-}DR^{-/lo}$ cells isolated from human cancer tissues but is not expressed by other immune cell populations, thus demonstrating the usefulness of methylglyoxal to identify human MDSCs. The rapid acquisition of MBo-fluorescence in T cells after 30 min of co-culture with MDSCs isolated from human cancer tissues further suggested that methylglyoxal was readily transmitted from MDSCs to T cells.

Methylglyoxal belongs to the family of α-dicarbonyls, a group of molecules with glycation capacity[49]. Dicarbonyls attack amino/guanidine-groups ($HN=C\text{-}(NH_2)\text{-}NH$), thus targeting preferentially the amino acids L-lysine and L-arginine as well as their residues in proteins to form advanced glycation end-products that can render amino acids and proteins non-functional[37, 50]. The amino acid L-arginine is essential for T cell activation and execution of effector functions[46, 51] and the depletion of free L-arginine, as well as modifications of proteins containing L-arginine is sufficient to block signaling and function of T cells [52, 53, 54].

Our results provide evidence that contact with MDSCs led to depletion of L-arginine within $CD8^{+}$ T cells. At the same time, we detected methylglyoxal-derived glycation products of L-arginine such as argpyrimidine and hydroimidazolone in T cells, which together suggests that MDSC-derived methylglyoxal caused intracellular depletion of L-arginine in T cells and thereby induced T cell paralysis. Methylglyoxal may suppress T cell function not only by chemical depletion of cytosolic amino acids like L-arginine but also by rendering L-arginine-containing proteins through glycation non-functional[37], such as protein kinases relevant for signal transduction or mitochondrial proteins involved in mitochondrial respiration[46, 55, 56, 57]. This intracellular depletion of arginine by methylglyoxal is a highly efficient and rapid mechanism to deprive $CD8^{+}$

T cells of their capacity to respond to activation signals and render them paralyzed, which is mechanistically distinct from expression of arginase that consumes extracellular arginine to deprive T cells of arginine sources[48].

Transfer of methylglyoxal from MDSCs to T cells required direct cell-cell contact, which may lead to a more pronounced T cell suppression at sites where MDSCs accumulate, such as tumor tissue. The identification of methylglyoxal as metabolic marker of MDSCs will allow to study which cells of the tumor micromilieu may be involved in the induction of MDSCs. Our observation that methylglyoxal-containing MDSCs were absent from secondary lymphoid tissues points towards a predominant local effect of immune suppression by MDSCs within tumor tissue, although MDSCs circulating in the blood may impair immune responses at distant sites from the tumor.

Based on this mechanistic insight, we were able to neutralize the glycation function of methylglyoxal with molecules containing amino/guanidine-groups or to prevent its formation by inhibiting SSAO enzymatic activity. Both measures abrogated the ability of MDSCs to paralyze CD8 T cells. Thus, methylglyoxal-mediated immune suppression by MDSCs is a promising molecular target for immune intervention to increase CD8 T cell immunity against cancer. Strikingly, we observed in a preclinical cancer model that neutralization of methylglyoxal with DMBG had a strong synergistic effect with checkpoint inhibition to strengthen cancer-specific CD8 T cell immunity. Since the combination treatment with DMBG/anti-PD1 did not increase numbers but the functionality of effector CD8 T cells in tumor tissue, the discovery of methylglyoxal as key immune suppressive mediator of intra-tumoral MDSCs opens new avenues for targeted immune intervention in cancer patients.

Acknowledgments

We thank J. Schulze, M. Beyer and S. Schmitt (Life and Medical Science Institute, University of Bonn, Germany) for isolating RNA and carrying out Illumina whole genome arrays; R. Weisskirchen (Institute of Molecular Pathobiochemistry, Experimental Gene Therapy and Clinical Chemistry, RWTH University Hospital Aachen, Germany) and J. Trebicka (Department of Internal Medicine I, University Clinic Bonn, Germany) for the kind providing of LX2 cells; Raul Berger (Institute of Molecular Immunology and Experimental Oncology, Technische Universität München, Munich, Germany) for performing seahorse experiments; C. Llanto, S. Michailidou and Silke Hegenbarth for their excellent technical support.

PK was supported by German Research Council (SFB TRR179) and German Center for Infection Research; BH was supported by the German Cancer Aid; TK was supported by the German Research Council (SFB1054, TR128, TR274, SyNergy (EXC 2145, ID 390857198)) and the ERC (CoG 647215).

Competing interests' statement: the authors declare to have no competing interests.

Author contributions

TB, AD, CS, SS, MH, KL, VL, UA, BLD, JS, LS, CF, NK, Tanja Bauer, ML, KE, SE, JEH, MA, MS, AH performed experiments and analyzed data; SD, JS, UA performed bioinformatic analyses; performed NH, DH BS, DS, FA, TM, HZ, MH, TK, CD, TH contributed specific technologies and reagents; BS, DS, TM, HS, MH, TK, CD, TH PM, PK and BH designed experiments; PJM, PAK, BH wrote the manuscript, all authors read and approved the manuscript.

Figure legends

Legend to Figure 1: Adjustment of cell metabolism to very low levels in human MDSCs compared to monocytes. **a**, differentially expressed genes encoding glycolysis KEGG-pathway enzymes in monocytes (left) compared to stromal cell-induced MDSCs (right; n = 3 independent biological samples). **b**, uptake of the glucose-analog 2-NBDG (n = 3) and Glut-1 cell surface expression levels (3 experiments). **c**, hexokinase activity (n = 3 independent biological samples). **d**, **e**, glucose uptake or hexokinase activity in $CD14^{+}HLA\text{-}DR^{+}$ (monocytes) or $CD14^{+}HLA\text{-}DR^{-/low}$ cells (MDSCs) from cancer patients (n =3 independent biological samples). **f**, extracellular acidification rate (ECAR) as measure of aerobic glycolysis (n = 3). **g**, mitochondrial mass (Mitotracker green) and mitochondrial membrane potential ($DilC_1(5)$), GeoMean given in numbers (n = 3 independent biological samples). **h**, oxygen consumption rate (OCR) as measure of mitochondrial respiration (n = 3 independent biological samples), statistical significance for baseline OCR. **i**, total cellular ATP content (n = 3 independent biological samples). **p < 0.01; ***p < 0.001; two-way unpaired t-test, diagrams plotted as SEM.

Legend to Figure 2: MDSCs suppress activation-induced signaling and consequently glycolysis and effector functions in CD8 T cells in a cell-contact dependent manner. Activated human $CD8^{+}$ T cells were co-cultured for 5 minutes (a), or 30 minutes (b and c, e-i) with MDSCs or monocytes (ratio 1:1), or human $CD14^{+}HLA\text{-}DR^{hi}$ monocytes or $CD14^{+}HLA\text{-}DR^{-/low}$ cells from cancer tissue (d). **a**, flow cytometric detection of activation-induced phosphorylation of signaling molecules in $CD8^{+}$ T cells co-cultured with MDSCs or monocytes at five minutes after anti-CD3/CD28 stimulation (n = 3 independent samples). **b**, fold change of surface Glut-1 expression and glucose uptake (n = 3 independent samples). **c**, fold-change of hexokinase activity of FACSorted $CD8^{+}$ T cells (n =3 independent samples). **d**, glucose uptake after co-culture with $CD14^{+}$ cells from cancer tissue (n = 3 independent samples). **e,** time kinetics of glycolytic rates. **f**, oxygen consumption rates (n = 3). **g**, fold change ATP levels (n = 3 independent samples) of FACSorted $CD8^{+}$ T cells. **h**, IFN-γ, TNF expression of activated $CD8^{+}CD45RA^{+}CX_3CR1^{+}$ T cells co-cultured with monocytes (red) or MDSCs (blue) (n = 3). **i,** proliferation of $CD8^{+}$ T cells in coculture with MDSCs or monocytes by CFSE- dilution or separation in transwell (0.4µm pore size). Numbers indicate division indices. (n = 8 independent samples). *p < 0.05; **p < 0.01; ***p < 0.001; two-way unpaired t-test; (F) ****p < 0.0001; two-way Anova, diagrams plotted as SEM.

Legend to Figure 3: Transfer of cytosolic constituents from MDSCs to CD8 T cells. a, Detection of MitoTracker Green fluorescence in $CD8^{+}$ T cells in co-culture (30 minutes) with MitoTracker Green-labeled MDSCs; transwell pore size 0.4 µm, MDSCs lysis by hypo-osmotic shock (n = 3 independent biological samples; results shown gated for CD8 T cells). **b**, transfer of cytosolic constituents from myeloid cells (Mitotracker) to $CD8^{+}$ T cells (eF670) after coculture for 30 minutes; scale bar 10 µm (n = 4 independent biological samples). **c**, quantification of transfer of cytosolic constituents to $CD8^{+}$ T cells by flow cytometry for monocytes (red) or MDSCs (blue) (n = 4 independent biological samples). **d**, transfer of cytosolic constituents from tumor-infiltrating $CD14^{+}$ cells of cancer patients, i.e. $HLA\text{-}DR^{hi}$ monocytes and $HLA\text{-}DR^{-/low}$ MDSCs labeled with MitoTracker, to $CD8^{+}$ T cells in co-culture (30 minutes), results

shown gated for $CD8^+$ T cells (n = 3 independent biological samples); most pronounced transfer into $CX_3CR1^+CD45RO^+$ effector $CD8^+$ T cells. **e**, no significant transfer of cytosolic constituents from MitoTracker-labeled primary human fibroblasts or keratinocytes to $CD8^+$ T cells in co-culture (30 minutes) (n = 3 independent biological samples). **f**, no transfer of myeloid cell surface markers to CD8 T cells (n = 3 independent biological samples). **g**, no detection of single nucleotide polymorphisms at position 152 of mitochondrial DNA from human MDSCs (donor) in lysates of $CD8^+$ T cells (acceptor). FACSorted after co-culture (30 minutes) (n = 5 independent biological samples separate donor acceptor experiments), demonstrating that no mitochondrial DNA was transferred from MDSCs to CD8 T cells thus excluding transfer of entire DNA-containing mitochondria.

Legend to Figure 4: Accumulation of dicarbonyl radical methylglyoxal is a metabolic marker for MDSCs and mediates their dormant metabolic phenotype. **a**, proliferation profiles of activated $CD8^+$ T cells after co-culture with MDSCs (blue) or MDSCs treated with rotenone (2 µM), or DMBG (200 µM) (purple) (n = 3). **b-j,** analyses of MDSCs. **b**, volcano plot (p-value vs. $\log_2$ fold-change) of 3-NPH-bound metabolites detected in MDSCs compared to monocytes by UHPLC-TOF-DIA-MS/MS (red arrow indicates methylglyoxal, feature ID: 67, see supplementary Table VII) (n = 6 independent samples). **c,** ion chromatograms of 3-NPH-bound methylglyoxal (exact mass of 3-NPH-bound methylglyoxal: 206.0579; tolerance: 0.01, n = 3). **d**, fluorescence intensity of the methylglyoxal-specific dye methyl-diaminobenzene-BODIPY (MBo) in MDSCs and monocytes and **e**, in tumor-infiltrating $CD14^+$ cells isolated from cancer patients (n = 3). **f**, MBo-fluorescence intensity in murine $CD11b^+$ cells from tumor tissue (B16-melanoma) or from the central nervous system during the recovery phase (day 22 after immunization) of experimental autoimmune encephalomyelitis (EAE) (n = 5). **g**, $CD14^+$ or $CD15^+$ cells were isolated from tumor tissue, liver tissue or blood from the same patient and examined for the expression of methylglyoxal (n = 2). **h**, MBo-fluorescence intensity in MDSCs after DMBG treatment (30 minutes) (n = 5). **i**, MBo-fluorescence and glucose-uptake in MDSCs (30 minutes pretreatment with inhibitors), note absent effect by robenidine that does not contain a guanidine-group (n = 3 independent samples). **j, k**, oxygen consumption and extracellular acidification rates of MDSCs (30 minutes DMBG pretreatment). OM = oligomycin, 2-DG = 2-deoxy-glucose, CCCP = carbonyl cyanide 3-chlorophenyl hydrazine (n = 3 independent samples). ***p < 0.001; two-way unpaired t-test; (F) ****p < 0.0001; two-way Anova, diagram plotted as SEM.

Legend to Figure 5: Methylglyoxal accumulates in MDSCs in a semicarbazide-sensitive-amine oxidase (SSAO) dependent fashion. b-e, analyses of human MDSCs. **a**, schematic illustration of the different pathways for generation of methylglyoxal in mammalian cells: spontaneous non-enzymatic dephosphorylation of glucose-derived dihydroxy-acetonephosphate; acetone monooxygenase (AMO) mediated enzymatic generation from fatty acid-derived acetol; SSAO mediated generation from glucose-derived and amino-acid-derived aminoacetone. **b**, metabolic pulse chase (6hrs) with 50% $^{13}C_6$-glucose and UHPLC-TOF-DIA-MC/MS analysis of MDSC lysates showing relative abundance of methylglyoxal isotopologues (technical triplicates, n = 2). **c**, *AOC3* mRNA level (coding for SSAO) in MDSCs and

monocytes (n = 2 independent biological samples). **d,** glyoxalase I (Glo-I) activity (n=5 independent biological samples). **e**, glutathione (GSH) quantification (n=5 independent biological samples). **f**, MBo-fluorescence intensity in MDSCs generated in the presence of inhibitors (72 hours): the monoamine-oxidase A inhibitor clorgyline (100 nM), the AMO inhibitor tetraethylthiuram-disulfid (TETD, 1 µM), and SSAO-specific inhibitors hydralazine (15 µM) and PXS-4681A (500 nM). Incubation of MDSCs with inhibitors for 2 hours exclude direct neutralization of methylglyoxal. DMBG used as a positive control that directly neutralizes glycation activity of methylglyoxal. (n = 4 independent biological samples). **g**, glucose uptake by MDSCs in presence of the above-mentioned inhibitors with the short incubation (2h) demonstrating that compounds did not have a direct effect on MDSCs. (n = 5). ns = not significant; *p < 0.05; **p < 0.01; ***p < 0.001; two-way unpaired t-test, diagrams plotted as SEM.

Legend to Figure 6: Guanidine-treatment of MDSCs abrogates their suppressive activity on CD8$^+$ T cell effector functions. a – f, analysis of human activated CD8$^+$ T cells in co-culture with MDSCs, that were pretreated (30 minutes) with indicated inhibitors. **a**, MBo-fluorescence in CD8$^+$ T cells after 10 minutes of coculture with MDSCs or monocytes (left) and glucose uptake (right) (n = 3 independent samples). **b**, intracellular cytokine staining of activated $CX_3CR1^+CD45RO^+$ CD8$^+$ T cells, (n = 3 independent samples). T cells were stimulated in the presence of MDSCs (pretreated with DMBG, methylguanidine, aminoguanidine or rodenidine (200µM), where mentioned), T cells were pretreated with DMBG, re-isolated after co-culture with MDSCs and stimulated after 1 or 4 hours, or DMBG treated after directly or after 1 hour. **c**, proliferation of activated CD8$^+$ T cells in co-culture with MDSCs or monocytes in presence of indicated compounds (CFSE-dilution, numbers denote division indices) (n = 3). **d**, CD14$^+$ or CD15$^+$ cells were isolated from tumor tissue, liver tissue or blood from the same patient were isolated an cocultured with CFSE labeled, activated CD8$^+$ T cells. Proliferation was measured by the dilution of CFSE (n = 2). **e**, **f**, free amino acids and advanced glycation products were measured using SIDA-UHPLC-MS/MSMRM in CD8$^+$ T cells after co-culture with MDSCs or monocytes. e, ion chromatogram of free L-arginine in CD8$^+$ T cells, g, quantification of amino acids L-glutamine and L-arginine and glycation products argpyrimidine, MG-H1 and MOLD (n = 4). ns = not significant; *p < 0.05; **p < 0.01; ***p < 0.001; two-way unpaired t-test, diagrams plotted as SEM.

Legend to figure 7: DMBG treatment overcomes MDSC-induced suppression of CD8$^+$ T cell function during therapeutic anti-cancer vaccination. a-g, at d10 after s.c. B16-OVA cancer cell inoculation, mice received ovalbumin adjuvanted with CpG/αGalCer, anti-PD-1 and/or DMBG in drinking water (40 mM), and analyses were performed at d17 (n = 5 mice). **a**, time kinetics of cancer growth in individual mice. **b**, **c**, MBo-fluorescence and glucose uptake of CD11b$^+$ cells from cancer tissue and spleen. **d**, CD8$^+$ T cell proliferation (CFSE-dilution) in co-culture with CD11b$^+$Ly6C$^+$ cells or CD11b$^+$Ly6G$^+$ (FACSorted) from cancer tissue or spleen (numbers denote division indices). **e - g**, MBo-fluorescence and glucose uptake *ex vivo* in CD8$^+$ T cells from tumor tissue or spleen. **h**, **i**, cytokine expression by CD8$^+$ T cells from cancer tissue after *ex vivo* ovalbumin peptide-specific stimulation. ns = not significant; data are presented as mean ± SEM, *p < 0.05; **p < 0.01; ***p < 0.001; two-way unpaired t-test, diagrams plotted as SEM.

References

1. Spitzer, M.H. *et al.* Systemic Immunity Is Required for Effective Cancer Immunotherapy. *Cell* **168**, 487-502 e415 (2017).

2. Williams, M.A. & Bevan, M.J. Effector and memory CTL differentiation. *Annual Rev Immunol* **25**, 171-192 (2007).

3. Togashi, Y., Shitara, K. & Nishikawa, H. Regulatory T cells in cancer immunosuppression - implications for anticancer therapy. *Nat Rev Clin Oncol* **16**, 356-371 (2019).

4. Veglia, F., Perego, M. & Gabrilovich, D. Myeloid-derived suppressor cells coming of age. *Nat Immunol* **19**, 108-119 (2018).

5. Ribas, A. & Wolchok, J.D. Cancer immunotherapy using checkpoint blockade. *Science* **359**, 1350-1355 (2018).

6. Hori, S., Nomura, T. & Sakaguchi, S. Control of regulatory T cell development by the transcription factor Foxp3. *Science* **299**, 1057-1061 (2003).

7. Bilate, A.M. & Lafaille, J.J. Induced CD4+Foxp3+ regulatory T cells in immune tolerance. *Annu Rev Immunol* **30**, 733-758 (2012).

8. Sugiyama, D. *et al.* Anti-CCR4 mAb selectively depletes effector-type FoxP3+CD4+ regulatory T cells, evoking antitumor immune responses in humans. *Proc Natl Acad Sci U S A* **110**, 17945-17950 (2013).

9. Bopp, T. *et al.* Cyclic adenosine monophosphate is a key component of regulatory T cell-mediated suppression. *J Exp Med* **204**, 1303-1310 (2007).

10. Nishikawa, H. & Sakaguchi, S. Regulatory T cells in cancer immunotherapy. *Current opinion in immunology* **27**, 1-7 (2014).

11. Bronte, V. *et al.* Recommendations for myeloid-derived suppressor cell nomenclature and characterization standards. *Nat Commun* **7**, 12150 (2016).

12. Huang, L.R. *et al.* Intrahepatic myeloid-cell aggregates enable local proliferation of CD8(+) T cells and successful immunotherapy against chronic viral liver infection. *Nat Immunol* **14**, 574-583 (2013).

13. Pallett, L.J. *et al.* Metabolic regulation of hepatitis B immunopathology by myeloid-derived suppressor cells. *Nat Med* **21**, 591-600 (2015).

14. Tcyganov, E., Mastio, J., Chen, E. & Gabrilovich, D.I. Plasticity of myeloid-derived suppressor cells in cancer. *Curr Opin Immunol* **51**, 76-82 (2018).

15. Kumar, V. *et al.* Cancer-Associated Fibroblasts Neutralize the Anti-tumor Effect of CSF1 Receptor Blockade by Inducing PMN-MDSC Infiltration of Tumors. *Cancer cell* **32**, 654-668 e655 (2017).

16. Hochst, B. *et al.* Activated human hepatic stellate cells induce myeloid derived suppressor cells from peripheral blood monocytes in a CD44-dependent fashion. *Journal of hepatology* **59**, 528-535 (2013).

17. Ostrand-Rosenberg, S. & Fenselau, C. Myeloid-Derived Suppressor Cells: Immune-Suppressive Cells That Impair Antitumor Immunity and Are Sculpted by Their Environment. *J Immunol* **200**, 422-431 (2018).

18. Klein Geltink, R.I. *et al.* Mitochondrial Priming by CD28. *Cell* **171**, 385-397 e311 (2017).

19. Chang, C.H. *et al.* Posttranscriptional control of T cell effector function by aerobic glycolysis. *Cell* **153**, 1239-1251 (2013).

20. Lu, Z. & Hunter, T. Metabolic Kinases Moonlighting as Protein Kinases. *Trends Biochem Sci* **43**, 301-310 (2018).

21. Menk, A.V. *et al.* Early TCR Signaling Induces Rapid Aerobic Glycolysis Enabling Distinct Acute T Cell Effector Functions. *Cell reports* **22**, 1509-1521 (2018).

22. Buck, M.D., Sowell, R.T., Kaech, S.M. & Pearce, E.L. Metabolic Instruction of Immunity. *Cell* **169**, 570-586 (2017).

23. Onfelt, B., Nedvetzki, S., Yanagi, K. & Davis, D.M. Cutting edge: Membrane nanotubes connect immune cells. *J Immunol* **173**, 1511-1513 (2004).

24. Watkins, S.C. & Salter, R.D. Functional connectivity between immune cells mediated by tunneling nanotubules. *Immunity* **23**, 309-318 (2005).

25. O'Neill, L.A. & Pearce, E.J. Immunometabolism governs dendritic cell and macrophage function. *J Exp Med* **213**, 15-23 (2016).

26. Ganeshan, K. & Chawla, A. Metabolic regulation of immune responses. *Annu Rev Immunol* **32**, 609-634 (2014).

27. El-Mir, M.Y. *et al.* Dimethylbiguanide inhibits cell respiration via an indirect effect targeted on the respiratory chain complex I. *J Biol Chem* **275**, 223-228 (2000).

28. Owen, M.R., Doran, E. & Halestrap, A.P. Evidence that metformin exerts its anti-diabetic effects through inhibition of complex 1 of the mitochondrial respiratory chain. *Biochem J* **348 Pt 3**, 607-614 (2000).

29. Wheaton, W.W. *et al.* Metformin inhibits mitochondrial complex I of cancer cells to reduce tumorigenesis. *Elife* **3**, e02242 (2014).

30. Teeter, M.E., Baginsky, M.L. & Hatefi, Y. Ectopic inhibition of the complexes of the electron transport system by rotenone, piericidin A, demerol and antimycin A. *Biochim Biophys Acta* **172**, 331-333 (1969).

31. Kinsky, O.R. *et al.* Metformin Scavenges Methylglyoxal To Form a Novel Imidazolinone Metabolite in Humans. *Chem Res Toxicol* **29**, 227-234 (2016).

32. Beisswenger, P. & Ruggiero-Lopez, D. Metformin inhibition of glycation processes. *Diabetes Metab* **29**, 6S95-103 (2003).

33. Han, J., Gagnon, S., Eckle, T. & Borchers, C.H. Metabolomic analysis of key central carbon metabolism carboxylic acids as their 3-nitrophenylhydrazones by UPLC/ESI-MS. *Electrophoresis* **34**, 2891-2900 (2013).

34. Allaman, I., Belanger, M. & Magistretti, P.J. Methylglyoxal, the dark side of glycolysis. *Front Neurosci* **9**, 23 (2015).

35. Wang, T., Douglass, E.F., Jr., Fitzgerald, K.J. & Spiegel, D.A. A "turn-on" fluorescent sensor for methylglyoxal. *J Am Chem Soc* **135**, 12429-12433 (2013).

36. Rabbani, N. & Thornalley, P.J. The dicarbonyl proteome: proteins susceptible to dicarbonyl glycation at functional sites in health, aging, and disease. *Ann N Y Acad Sci* **1126**, 124-127 (2008).

37. Rabbani, N., Xue, M. & Thornalley, P.J. Methylglyoxal-induced dicarbonyl stress in aging and disease: first steps towards glyoxalase 1-based treatments. *Clin Sci (Lond)* **130**, 1677-1696 (2016).

38. Phillips, S.A. & Thornalley, P.J. The formation of methylglyoxal from triose phosphates. Investigation using a specific assay for methylglyoxal. *Eur J Biochem* **212**, 101-105 (1993).

39. Ohmori, S., Mori, M., Shiraha, K. & Kawase, M. Biosynthesis and degradation of methylglyoxal in animals. *Progress in clinical and biological research* **290**, 397-412 (1989).

40. Ray, S. & Ray, M. Formation of methylglyoxal from aminoacetone by amine oxidase from goat plasma. *J Biol Chem* **258**, 3461-3462 (1983).

41. Lyles, G.A. & Chalmers, J. The metabolism of aminoacetone to methylglyoxal by semicarbazide-sensitive amine oxidase in human umbilical artery. *Biochem Pharmacol* **43**, 1409-1414 (1992).

42. Mizukoshi, E. *et al.* Myeloid-derived suppressor cells correlate with patient outcomes in hepatic arterial infusion chemotherapy for hepatocellular carcinoma. *Cancer Immunol Immunother* **65**, 715-725 (2016).

43. Gao, X.H. *et al.* Circulating CD14(+) HLA-DR(-/low) myeloid-derived suppressor cells predicted early recurrence of hepatocellular carcinoma after surgery. *Hepatol Res* **47**, 1061-1071 (2017).

44. Arihara, F. *et al.* Increase in CD14+HLA-DR -/low myeloid-derived suppressor cells in hepatocellular carcinoma patients and its impact on prognosis. *Cancer Immunol Immunother* **62**, 1421-1430 (2013).

45. Bronte, V., Serafini, P., Mazzoni, A., Segal, D.M. & Zanovello, P. L-arginine metabolism in myeloid cells controls T-lymphocyte functions. *Trends Immunol* **24**, 302-306 (2003).

46. Geiger, R. *et al.* L-Arginine Modulates T Cell Metabolism and Enhances Survival and Anti-tumor Activity. *Cell* **167**, 829-842 e813 (2016).

47. Gabrilovich, D.I., Ostrand-Rosenberg, S. & Bronte, V. Coordinated regulation of myeloid cells by tumours. *Nat Rev Immunol* **12**, 253-268 (2012).

48. Gabrilovich, D.I. Myeloid-Derived Suppressor Cells. *Cancer Immunol Res* **5**, 3-8 (2017).

49. Rabbani, N. & Thornalley, P.J. Dicarbonyl stress in cell and tissue dysfunction contributing to ageing and disease. *Biochem Biophys Res Commun* **458**, 221-226 (2015).

50. Nemet, I. & Varga-Defterdarovic, L. Methylglyoxal-derived beta-carbolines formed from tryptophan and its derivates in the Maillard reaction. *Amino Acids* **32**, 291-293 (2007).

51. Murray, P.J. Amino acid auxotrophy as a system of immunological control nodes. *Nat Immunol* **17**, 132-139 (2016).

52. Chantranupong, L. *et al.* The CASTOR Proteins Are Arginine Sensors for the mTORC1 Pathway. *Cell* **165**, 153-164 (2016).

53. Saxton, R.A., Chantranupong, L., Knockenhauer, K.E., Schwartz, T.U. & Sabatini, D.M. Mechanism of arginine sensing by CASTOR1 upstream of mTORC1. *Nature* **536**, 229-233 (2016).

54. Wang, S. *et al.* Metabolism. Lysosomal amino acid transporter SLC38A9 signals arginine sufficiency to mTORC1. *Science* **347**, 188-194 (2015).

55. Cheng, C.T. *et al.* Arginine starvation kills tumor cells through aspartate exhaustion and mitochondrial dysfunction. *Commun Biol* **1**, 178 (2018).

56. Taheri, F. *et al.* L-Arginine regulates the expression of the T-cell receptor zeta chain (CD3zeta) in Jurkat cells. *Clin Cancer Res* **7**, 958s-965s (2001).

57. Qiu, F. *et al.* Arginine starvation impairs mitochondrial respiratory function in ASS1-deficient breast cancer cells. *Sci Signal* **7**, ra31 (2014).

Methods

Animal models and therapeutic vaccination

All animal experiments were performed according to the federal German law regarding the protection of animals (ROB-55.2-2532.Vet_02-193 & ROB-55.2-2532.Vet_02-17-234). C57Bl/6J mice, H2-K^{bSIINFEKL} restricted TCR-transgenic animals (OT-I) and LysM-Cre/B6;129-Gt(ROSA)26Sor$^{tm4(CAG-EGFP)Nat}$/JRosa-mitoGFP (Jackson stock: 004781[60]; Jackson stock: 021429[61]) were bred according to the FELASA guidelines. B16-OVA cells, obtained from A.-K. Heine, Institute of Experimental Immunology, University of Bonn, were cultured in DMEM media containing 10% FCS, 200 mg/ml penicillin, 200 U/ml streptomycin, 2 mM L-glutamine and 400 µg/ml G418. For tumor implantation, 5×10^5 B16 melanoma cells were injected subcutaneously into the left flank. Tumor size was measured using digital caliper and tumor volume was calculated using the ellipsoid formula $V = \frac{4}{3}\pi r^2$. After 10 days, mice were either vaccinated using 200 µg ovalbumin with 20 µg CpG-oligonucleotide 1668 (TBI Mol) and 0.2 µg α-galactosylceramide (Axxora) in 100 µl PBS. DMBG was administrated via drinking water (40 mM). Anti-PD-1 (clone 29.F1A12) was applied i.p. every 3rd day (200 µg). Experimental autoimmune encephalomyelitis was induced by subcutaneous application of 200 µg MOG(35-55) peptide (MEVGWYRSPFSRVVHLYRNGK) and 500 µg *Mycobacterium tuberculosis* H37Ra in Freund´s adjuvant oil with additional intravenous injection of 200 ng pertussis toxin on day 0 and 2, as previously described[62].

Antibodies

The following antibodies were used experiments with human cells: anti-CD1c (L161), anti-CD3 (HIT3a), anti-CD4 (OKT4), anti-CD8 (SK1), anti-CD11c (3.9), anti-CD14 (63D3), anti-CD16 (3G8), anti-CD19 (HIB19), anti-CD20 (2H7), anti-CD24 (ML5), anti-CD25 (BC96), anti-CD27 (M-T271), anti-CD38 (HB-7), anti-CD40 (5C3), anti-CD45RA (HI100), anti-CD45RO (UCHL1), anti-CD56 (5.1H11), anti-CD62L (DREG-56), anti-CD95 (DX2), anti-CD123 (6H6), anti-CD127 (A019D5), anti-CD158 (HP-MA4), anti-CD197 (G043H7), anti-CD274 (29E.2A3), anti-CD303 (201A), anti-CD314 (1D11) anti-IgM (MHM-88), anti-IgG (HP6017), anti-HLA-DR (L243), anti-TNF (Mab11), anti-IFN-γ (4S.B3), anti-Granzyme b (GB11), anti-Glut-1 (polyclonal, Novus Biologicals), anti-CX3CR1 (2A9-

1), anti- phospho-Zap70 (n3kobu5), anti-phospho-LCK (SRRCHA), anti-phospho-AKT (SDRNR), anti-phospho-mTOR (MRRBY), anti-phospho-ERK (MILAN8R). For mice, the following antibodies were used: anti-CD3 (145-2C11), anti-CD4 (RM4-5), anti-CD8 (53-6.7), anti-CD11b (M1/70), anti-CD11c (N418), anti-Ly6C (4K1.4), anti-Ly6G (1A8) anti-F4/80 (BM8), anti-I-A/I-E (M5/114.15.2), anti-NK1.1 (PK136), anti-B7-H1 (10F.9G2), anti-IFN-γ (XM61.2), anti-TNF (MP6-XT22) anti-CD25 (PC61), anti-Foxp3 (FJK16S), anti-CD62L (MEL-14), anti-CD44 (IM7), anti-CD45.1 (A20), anti-CD45.2 (104), anti-MerTK (2B10C42). If not otherwise specified, antibodies were from Sony Biotechnology or BioLegend.

Flow cytometry and FACSorting

The phenotype of immune cells was determined by multicolor flow cytometry using a Sony SP6800 or Sony SA3800 spectral analyzer (both Sony Biotechnology). FACS-Sorting of cells was done using a Sony SH800 cell sorter. Data were analyzed using FlowJo software 10.0.8 (TreeStar Inc.)

Immune cell isolation and culture

All experiments with human blood or human liver samples were performed in accordance to the ethic votes 434/17S, 564/18SAS and 232/19S. Informed written consent was obtained from each patient. Peripheral blood mononuclear cells (PBMCs) were isolated from freshly drawn blood by density gradient centrifugation. Splenic and tumor infiltrating cells in mice were isolated as described previously [58]. If not specified, chemicals and kits were purchased from ThermoFisher Scientific or Sigma Aldrich. Briefly, immune cells were isolated from spleen and tumor tissues by mechanical disruption and tumor tissue was further digested with 0.1% collagenase (Sigma-Aldrich) in RPMI for 10 min at 37°C. Single cells were isolated using 40% percoll (GE Healthcare) and Ficoll density gradient centrifugation. Monocytes and $CD8^+$ T cells were further purified by immunomagnetic separation using anti-CD8 or anti-CD11b microbeads and AutoMACS (Miltenyi Biotech), followed by FACS-Sort gating on $CD11b^+Ly6C^+$ or $CD11b^+Ly6G^+$ cells.

Human tumor tissue was mechanically shredded followed by enzymatic digestion with 0.1% collagenase and 0.1% DNase in RPMI at 37°C for 30 min. Single cells were isolated using 40%

746 percoll (GE Healthcare) and Ficoll density gradient centrifugation. Monocytes and $CD8^+$ T cells
747 were further purified by immunomagnetic separation using anti-CD8 or anti-CD14 microbeads
748 and AutoMACS (Miltenyi Biotech). MDSCs and monocytes were isolated from peripheral blood
749 mononuclear cells by FACS-Sort gating on $CD14^+HLA\text{-}DR^{-/lo}$ or $CD14^+HLA\text{-}DR^+$ cells.
750
751 ## Induction of human MDSCs from monocytes by stromal cells
752 Human monocytes (10^6) isolated from peripheral blood of healthy volunteers were cultured on a
753 confluent layer of human stromal liver cells, i.e. myofibroblast cells (LX2)[59] (4×10^5 cells in 24-
754 well plates) in RPMI supplemented with penicillin (200 mg), streptomycin (200 U/ml), L-
755 glutamine (2 mM) and 10% FCS for three days without medium change. Viable MDSCs were
756 separated from myofibroblasts by FACS-Sorting before use in functional assays. MDSCs
757 generated from monocytes were characterized by downregulation of HLA-DR and their capacity
758 to inhibit proliferation of anti-CD3/CD28 activated $CD8^+$ T cells. Where indicated, 100 nM (2,4-
759 dichlorophenoxy)-N-methyl-N-prop-2-ynylpropan-1-amine hydrochloride), 1 μM TETD,
760 (diethylcarbamothioylsulfanyl N, N-diethylcarbamodithioate), 15 μM phthalazine-1-ylhydrazine,
761 50 nM PXS-4681A ((E)-2(aminomethyl)-3-fluoroprop-2-enoxy)-benzenesulfonamide) or 200 μM
762 dimethylbiguanide (DMBG), methylguanidine, aminoguanidine, (4-Chlorphenyl)-5-
763 isopropylbiguanid or tolylbiguanide were added during the co-culture with stromal cells.
764
765 ## T cell proliferation assay
766 Isolated $CD8^+$ T cells and $CD14^+$ cells were co-cultured at a ratio 1:1 and T cells were activated
767 with anti-CD3/CD28 coated Dynabeads (1 μl/ 10^6 cells; 4×10^4 beads / 10^6 cells). As indicated,
768 cells were labeled with carboxyfluorescein-succinimidyl-ester (CFSE) for quantitative
769 determination of proliferation or cells were incubated for 4 h with monensin/brefeldin A when
770 subjected to intracellular cytokine staining. Where indicated, cells were treated with L-NO-
771 hydroxyl-L-arginine (L-NOHA) (10 μM), L-NG-monomethyl-L-arginine (L-NMMA) (10 μM),
772 Mn(III)tetrakis(4-benzoic acid)porphyrin Chloride (MnTBAP) (40 μM), 1-MT (20 μM), anti-TGF-β
773 (1D11), anti-IL-10 (JES3-19F1), anti-PD-1 (EH12.2H7) (40 μg/ml each), retinoic acid (500 nM),
774 DMBG (200 μM), methylguanidine, aminoguanidine, (4-Chlorphenyl)-5-isopropylbiguanid or

tolylbiguanide (200 μM) 3-bromopyruvate (60 μM) or rotenone (2 μM). Proliferation was determined by dilution of CFSE and division/proliferation index were calculated using FlowJo 10.4.2.

Measurement of specific analytes

Arginase assay. Immune cells were isolated, washed twice with PBS and resuspended in 50 μl water containing 0.1% Triton-X and protease inhibitor mixture (Roche Molecular Diagnostics) and incubated for 30 min at 37°C. 50 μl Tris-HCl (pH 8; 25 mM) containing 333 μM MnCl2 was added followed by heating up the mixture up to 56°C for 10 min. 100 μl of L-Arginine solution (0.5 M) (Sigma-Aldrich) was added and the samples were incubated at 37°C for 30 min. The hydrolysis reaction was stopped by adding 10% H_2SO_4 and 25% H_3PO_4 in H_2O. 40 μl α-isonitrosopropiophenone was added, heated up to 96°C for 45 min. Urea concentration was determined by absorbance at 540 nm using a Tecan Reader.

NO-and ROS measurement. NO was measured using the modified Griess reagent (Sigma) and ROS production was measured by using 5 μM 2,7-Dichlorofluorescin diacetate (H_2DCFDA) according to the manufacturer's protocol.

Cytokine measurement in supernatants. Cytokine quantification was done using ELISA for IL-1β, IL-6, IL-10 and TNF (all BioLegend) according to the manufacturer's protocol.

Hexokinase colorimetric assay. The activity of hexokinase in cellular lysates was analyzed by measuring the NADH production per time in a colorimetric assay according to the manufacturer's protocol.

ATP assay. The ATP level of cells was analyzed using the ATP Assay Kit according to the manufacturer's protocol.

Glucose uptake assay. Cells were cultured in glucose-free RPMI and incubated with 10 μM (2-N-(7-Nitrobenz-2-oxa-1,3-diazol-4yl)-Amino)-2-Deoxyglucose (2-NBDG) for 30 min followed by determination of 2-NBDG fluorescence intensity by flow cytometry.

Glyoxalase assay. The enzymatic activity of glyoxalase I was measured using the "Glyoxalase I Activity Assay Kit" from Sigma and is based on the change of absorbance at 240 nm due to the conversion of methylglyoxal (substrate) to S-lactoylglutathione in the presence of reduced glutathione (co-substrate). Briefly, cell pellets were permeabilized in assay buffer supplemented with 0.1% Triton-X for 5 min at 21°C in an UV-transparent 96-well plate. Assay buffer containing substrate and co-substrate was added and the increase of absorbance at 240 nm within 20 min was measured to calculate the enzymatic activity. The activity was normalized to the protein concentration of the sample, as measured with a standard colorimetric protein assay (Bio-Rad, Laboratories Inc.).

Immunoblot

$CD8^+$ T cells were stimulated with CD3/CD28 antibodies and either left alone or co-cultured in the presence of monocytes or MDSCs for different periods of time. Subsequently, cells were lysed in buffer containing 1% lauryl maltoside (LM) (N-dodecyl β-maltoside), 1% NP-40, 1 mM Na_3VO_4, 1 mM PMSF, 10 mM NaF, 10 mM EDTA, 50 mM Tris pH 7.5, and 150 mM NaCl for 20 min on ice. Lysates were centrifuged and supernatants were incubated at 99°C for 5 min in sample buffer containing β-mercaptoethanol before SDS-PAGE. Proteins were transferred onto a nitrocellulose membrane (Amersham) and blocked with TBS containing 5% milk for 1 h at 21°C The following antibodies were used to detect phosphorylated proteins: phospho-Zap70 (Tyr319), phospho-LAT (Tyr191), phospho-PLC-γ1 (Tyr783), and phospho-Erk1/2 (Thr202/Tyr204) (all from Cell Signaling). An anti-β-actin antibody (clone AC15) was used to show equal loading. Membranes were subsequently incubated with HRP-labeled secondary antibodies for 1 h and phosphorylated proteins were detected using the ECL system (Amersham).

Bioenergetics measurements

Immune cells were seeded on a Seahorse 96-well plate (10^5 cells/well) in unbuffered RPMI medium, containing 10 mM glucose and 2 mM glutamine and additionally supplemented with 2 mM glutamine and manually adjusted to pH 7.4. For oxidative profiling, 2 μM oligomycin to block ATP synthesis, 1.5 μM CCCP to uncouple mitochondria proton pumping and 2 μM antimycin A and rotenone each to block electron transport chain, were injected during measurement of oxygen consumption rates (OCR) in a Seahorse XF 96 Analyzer (Agilent Technologies). For glycolytic profiling, immune cells were seeded in unbuffered, glucose-free DMEM (Seahorse Bioscience, Agilent Technologies), manually adjusted to pH 7.4. Glycolysis, monitored as extracellular acidification rate (ECAR), was started after addition of 10 mM glucose, followed by 1 μM oligomycin to block mitochondrial ATP synthesis and 20 mM deoxyglucose (DG) that reduces ECAR to glycolysis-unrelated levels. Glycolytic reserve was calculated as difference of ECAR after oligomycin injection and baseline ECAR. ATP-linked respiration states the difference between OCR after oligomycin injection and baseline. LPS (100 ng/ml) and PMA (50 μg/l) were injected to monitor the glycolytic switch in T cells. If not specified chemicals and medium were obtained from Merck, Sigma-Aldrich.

ELISPOT for detection of Granzyme B secretion

Granzyme B secretion was measured on 1×10^5 isolated T cells stimulated with 2 μg/ml CEF peptide pool (Cytomegalovirus (CMV), Epstein-Barr (EBV) and Influenza virus (Flu)) (Proimmune) using the human Granzyme B ELISpot^{plus} Kit (Mabtech AB, NACKA Strand, Sweden) according to the manufacturer`s instructions. ELISpot plates were evaluated within three days after assay performance using an automated reader system (CTL-ImmunoSpot® S6 Ultra-V Analyzer/CTL ImmunoSpot 5.4 Professional DC Software, CTL Europe). Scanning and counting of ELISpot plates was performed with automatically adjusted settings conducted by the reader. All obtained counts were reviewed and certified by a second person during a quality control process.

Mitochondrial staining

Cells were stained using 200 nM Benzoxazolium,2-[3-[5,6-dichloro-1,3-bis[[4-(chloromethyl)phenyl]methyl]-1,3-dihydro-2H-benzimidazol-2-ylidene]-1-propenyl]-3-methyl-

chloride (Mitotracker-Green) or 50 nM Mito-Probe 3H-Indolium, 2-(5-(1,3-dihydro-1,3,3-trimethyl-2H-indol-2-ylidene)-1,3-pentadienyl)-1,3,3-trimethyl-iodide 36536-22-8 (DICL1(5)) according to the manufacturer's protocol.

Methylglyoxal detection at single cell level by flow cytometry

The fluorescent sensor methyl diaminobenzene-BIODIPY (MBo), that specifically detects methylglyoxal[35], was used to detect presence of methylglyoxal at the level of single cells using flow cytometry. Cells were loaded with MBo (10 μM) for 30 minutes in RPMI (supplemented with 10% FCS, 200 mg penicillin, 200 U/ml streptomycin and 2 mM L-glutamine) at 37°C, washed and subjected to further cell surface antibody staining before flow cytometric evaluation.

RNA isolation and quantitative PCR

RNA was isolated using RNeasy Kit (Qiagen) and complementary DNA synthesis was done with Superscript Velo (ThermoFisher) according to the manufacturer´s instructions. Quantitative PCR was performed with SYBR-Green (Roche Molecular Diagnostics) using the following primers: *CYPA* forward: 5´-ATGCTCAACCCCACCGTGT-3´; *CYPA* reverse: 5´-TCTGCTGTCTTTGGGACCTTGTC-3´, *TGFB* forward: 5´- gtggaaacccacaacgaaat-3´; *TGFB* reverse: 5´-CACGTGCTGCTCCACTTTTA-3´, *IDO1* forward: 5´-AGAGTCAAATCCCTCAGTCC-3´; *IDO1* reverse: 5´-AAATCAGTGCCTCCAGTTCC-3´; *AOC3* forward: 5´-GGAACCAAGTGTCAGAGCACA-3´; *AOC3* reverse: 5´-GGACAAAGACCATATCCTCGGC-3´; *SERPINB14*) forward: 5´-TGTTGGTGCTGTTGCCTGATG-3´; *SERPINB14* reverse: 5´-TTGGTTGCGATGTGCTTGATAC-3´. Samples were analyzed in triplicates and normalized to endogenous *CYPA* mRNA abundance.

Gene expression profiling of monocytes and MDSCs and bioinformatic analysis

After 18 h of co-culture of human monocytes with stromal cells, myeloid cells were separated from stellate cells by FACSorting. RNA was isolated from 5×10^6 cells using TRIzol according to the manufacturer's protocol. Biotin-labeled cRNA was generated using the TargetAmp Nano-g Biotin-cRNA labeling Kit (Epicentre). Biotin labeled cRNA was generated using the TargetAmp Nano-g Biotin-cRNA Labeling Kit for the Illumina System (Epicentre). cRNA was hybridized onto

Illumina HumanRef-12 (version 3) bead array that probed for 48,794 genes. The raw intensity values were analyzed using Genome Studio. The probe intensities from Illumina HumanRef-12 gene chip were imported into the R environment (http://www.r-project.org./). The probes were normalized using robust spline normalization (RSN) method in lumi-R-package[63]. The differentially expressed genes (DEGs) were identified using the Bioconductor package Limma[64]. We considered a particular gene as a DEG when its expression $\log_2$ fold change 0.6 (absolute fold change 1.5, corrected p-value (q-value) ≤ 0.05). Pathway enrichment analysis of DEGs was performed using METASCAPE (accessed on 13/06/16, http://metascape.org)[65]. Cell surface proteome analysis was performed by comparing differently expressed genes in MDSCs with the human cell surface proteome database (http://wlab.ethz.ch/cspa)[66].

Mitochondrial DNA detection

$CD8^+$ T cells ("acceptor") or monocytes ("donor") were purified from the blood of two non-related, healthy individuals. After 30 min of co-culture, viable $CD8^+$ T cells were separated using a SH800 cell sorter (Sony (Sony Biotechnology) in ultra-purity mode and whole DNA was isolated. mtDNA was amplified via XL-PCR (single amplicon 16569 bp) and sequenced with an Illumina MiSeq (Illumina Inc.). Donor specific homoplasmic single nucleotide polymorphism (SNP) were identified and used to test for trans-cellular mtDNA transfer from donor to acceptor cells. To control for contamination with donor cells due to false-sorting, donor-specific microsatellites of nuclear DNA were analyzed. No contamination was detected, the limit of detection was approximately 2%.

Confocal live cell microscopy

For live cell imaging, a PerkinElmer UltraVIEW VoX spinning disc microscope with Nikon TiE equipped with the Hamamatsu EM-CCD ImagEM X2 camera, APO TIRF 60x NA1.49 oil immersion objective and environment control system (37°C and 5% CO_2), was used. T cells were stained with eF670 (1 µM) and monocytes with Mitotracker green (200 nM) for 15 min and placed in 8-well glass bottom chambered slides (Ibidi) in imaging medium (RPMI). Chambered slides were placed on the microscope and focus was "locked-in" using hardware-based autofocusing system.

Then, monocytes were added to the chambers and time-lapse acquisition started. The entire 3D volume of cells was acquired by optical sectioning using piezo *z*-drive step of 0.5 µm (15 steps) every 75 sec for a total imaging duration between 40-60 min. eF670 and Mitotracker green were imaged using 640 nm laser with 705/90 filter and 488 nm laser with 525/50 filter, respectively. Transmission (DIC) images were acquired in addition.

For ultra-structural analysis during live cell imaging, LSM 880 Airyscan and Airyscan FAST, respectively, equipped with a Plan-Apochromat 63x NA1.2 water immersion objective was used (Carl Zeiss Microscopy GmbH). T cells and monocytes were isolated. Monocytes were stained with Mitotracker green (200 nM) and placed in 8-well glass bottom chambered slides (Ibidi) in the imaging medium (RPMI). Then, monocytes were added to the chambers and time-lapse acquisition started. The entire 3D volume of cells was acquired by optical sectioning using piezo *z*-drive step of 0.173 µm (45 steps, total range of 7.6 µm) every 53 sec for a total imaging duration of 1 h 28 min. Cells were imaged including nuclear staining, laser-DIC and MitoTracker green using 405 nm, 488 nm and 633 nm lasers with emission bands of 420-480 nm (nuclear stain) and 495-550 nm (MitoTracker green), respectively. Laser-DIC was added in an additional track at 633 nm laser for optimized penetration depth at minimal bleaching. Images were acquired at two-fold optical zoom resulting in 67.5 × 67.5 μm^2 at a pixel size of 0.04 × 0.04 μm^2.

UHPLC-TOF-DIA-MS/MS analysis

Monocytes an MDSCs were isolated or induced as described above. For ^{13}C-labeling experiments, medium containing 50% $^{13}C_6$-Glucose (Merck) was used during induction of MDSCs.

Isolated cells were transferred into CK14 – 0.5 mL bead beater tubes (Bertin Technologies) containing 1.4 mm diameter ceramic (zirconium oxide) beads. After addition of acetonitrile/water (250 µL, 50/50, v/v), the samples were homogenized for 3 × 30 sec with 20 s breaks between at 7,800 rpm (Precellys Evolution Homogenizer, Bertin Technologies); to prevent excessive heating during homogenization, samples were cooled with liquid nitrogen using a Cryolys cooling system (Bertin Technologies). Subsequently, samples were equilibrated for 15 min at 21°C and centrifuged at 16,100 g and 4°C for 5 min (Centrifuge 5415 R, Eppendorf) and the clear supernatant was stored at -80°C until further analysis. For derivatization, 40 µl of the

cell extract were mixed with 20 µl of a solution of 3-nitrophenyl hydrazine (200 mM, 50:50, v/v, ACN/H_2O) and 20 µl of a 120 mM solution of N-(3-Dimethylaminopropyl)-N'-ethylcarbodiimide in 6 % pyridine (50:50, v/v, ACN/H_2O) and reacted for 30 min at 40 °C. Afterwards the mixture was diluted with ACN/ H_2O (200 µl, 50:50, v/v) and used directly for UHLC hyphenated with time-of flight (TOF) mass spectrometry (MS) and fragment spectra were acquired by means of data independent acquisition (DIA). For the analysis, an Nexera X2 UHPLC system (Shimadzu) consisting of two LC-30AD pumps, a SIL-30AC auto sampler, a CTO-30A column oven and a CBM-20A system controller was connected to 6600 TripleTof instrument (Sciex) equipped with an IonDrive ion source (Sciex) operating in negative electrospray mode. After each fifth sample the instruments calibration was verified and corrected using ESI Negative Calibration solution (Sciex) and a Calibrant Delivery System (Sciex). UHPLC separation was performed on a Kinetex Phenyl-Hexyl column (100 mm x 2.1 mm, 1.7 µm Phenomenex) using water (mobile phase A) and acetonitrile (mobile phase B) with 0.1% formic acid each and the following gradient program: 0 min 36% B, 2 min 36% B, 3.5 min 80% B, 5 min 100% B, 7 min 100% B, 8 min 36% B, 12 min 36% B. The total flow of the chromatography was set to 0.25 mL/min and separation was performed at 40°C. The mass spectrometer was operated in the SWATH mode with a series of 19 consecutive experiments per 1.05 sec measurement cycle. After starting with a high-resolution scan of the intact precursor ions from 50 to 1000 m/z for 100 ms, fragment ions were generated by means of collision-induced fragmentation subsequently for precursor ions within 18 separate windows ranging from 50 to 600 m/z (window width 30 Da each, 1 Da overlap), the resulting fragment spectra were recorded in the high sensitivity mode (50 ms acquisition per window). Ion spray voltage was set at -4500 V and the following source parameters were applied: curtain gas 35 psi, gas 1 55 psi, gas 2 65 psi, temperature 500°C. Declustering potential was set to 80 V for all experiments while the collision energy was 10 V for precursor ion scans and 35 V including 25 V collision energy spread for the fragmentation in the individual SWATH windows. The following compounds, have been measured as references: 3-phosphoglycerat, fructose-6-phosphate, fructose-1,6- diphosphate, glucose, glucose-6-phosphate, glutathione, glyoxal, lactate, lactoylglutathione, methylglyoxal, nucleotide mix, organic acid mix, phosphoenolpyruvate, pyruvate.

975

976 **Quantification of amino acids (AAs) and advanced glycation products (AGPs) by stable isotope**
977 **dilution analysis (SIDA-UHPLC-MS/MS).**

978 Amino acids (AAs) L-arginine (**1**), L-glutamine (**2**), L-methionine (**3**), L-asparagine (**4**), L-glutamic
979 acid (**5**), L-tyrosine (**6**), L-isoleucine (**7**), L-phenylalanine (**8**), L-lysine (**9**), L-serine (**10**), L-leucine
980 (**11**), L-tryptophan (**12**), L-aspartic acid (**13**) and L-alanine (**14**) as well advanced glycytion
981 products (AGPs) argpyrimidine (**15**), MG-H1 (**16**), imidazolysine (**17**), pyrraline (**18**),
982 carboxyethyllysine (**19**) and carboxymethyllysine (**20**) were analysed by means of two newly
983 developed SIDA-UHPLC-MS/MS_{MRM} methods separately. To this end, corresponding stable
984 isotope labelled AA standards L-arginine (^{13}C6-**1**), L-glutamine ($^{13}C_5$-**2**), L-methionine (methyl-d_3-
985 **3**), L-asparagine ($^{15}N_2$-**4**), L-glutamic acid ($^{13}C_5$-^{15}N-**5**), L-tyrosine (ring-d_4-**6**), L-isoleucine ($^{13}C_6$-**7**),
986 L-phenylalanine (ring-d_5-**8**), L-lysine ($^{13}C_6$-**9**), L-serine ($^{13}C_3$-**10**), L-leucine ($^{13}C_2$-**11**), L-tryptophan
987 (indole-d_5-**12**), L-aspartic acid ($^{13}C_4$-^{15}N-**13**) and L-alanine ($^{13}C_3$-**14**) as well imidazolysine-$^{15}N_2$ (**17**-
988 $^{15}N_2$), MG-H1-d_3 (**16**-d_3) for AGP analysis were utilized. AGPs were obtained from Iris-Biotech.
989 Stable isotope labelled AAs were bought from Cambridge Isotopes. Solvents used for LC-MS/MS
990 analysis were of LC-MS grade (Honeywell). Ultrapure water for UHPLC separation and mass
991 spectrometry was purified by means of a Milli-Q water advantage A 10 water system (Millipore).
992 Millipore-grade water was used for all experiments unless stated otherwise.

993

994 *Internal Standard (IS)*

995 Internal standards were prepared in stock solutions (500 µL) with concentrations given in
996 supplementary Table VIII and were prepared in ACN/H_2O (10/90, v/v). Iimidazolysine-$^{15}N_2$ (12.06
997 mmol/L, **17**-$^{15}N_2$) and MG-H1-d_3 (13.1 mmol/L, **16**-d_3) were dissolved in D_2O and their exact
998 concentration was verified by means of quantitative NMR (qNMR) and it was stored at −20 °C
999 until used. Internal standard solutions for amino acid (AA) and advanced glycation product (AGP)
1000 analysis were prepared by diluting stock solutions 1:5 and 1:20 with ACN/H_2O (50/50, v/v),
1001 respectively.

1002

1003 *Sample preparation*

Cells were lysed at 0°C by bead beater (Precellys Evolution Homogenizer, Bertin) at 7000 rpm for 6 × 20 sec with 30 sec pause in between. Afterwards lysed cells were ultrafiltrated (Amicon Ultra, Merck, 3 kDa centrifugal filters; 13,600 × g, 30 min, 4 °C). Filtrates were dried by vacuum centrifugation (Eppendorf Concentrator Plus, 6 h, 30°C), solved in 100 µL H_2O, internal standard solutions (each 2 µL) were added and subjected to the UHPLC-MS/MS system. Recovered protein was eluted by centrifugation (1,000 × g, 5 min, 4 °C). According to Ahmed, Argirov [67] and Salomón, Sibbersen [68] hydrolysis was carried out with slight modifications. Protein samples were mixed with HCl (aq, 40 mM, 50 µL), thymol solution (1 mg/mL in 40 mM HCl, 10 µL) and pepsin solution (1 mg/mL in 40 mM HCl, 10 µL) and incubated at 37°C for 24 h in an Eppendorf Thermomixer at 400 rpm. Subsequently, each sample was buffered and neutralized by addition of sodium phosphate buffer (aq., 500 mM, 50 µL) and sodium hydroxide (aq., 260 mM, 9 µL). Further hydrolysis was conducted by Pronase E (1 mg/mL in 10 mM sodium phosphate buffer, 10 µL) for 24 h at 37°C in an Eppendorf Thermomixer at 400 rpm. In the last hydrolysis step, leucine aminopeptidase and prolidase (each 1 mg/mL in 10 mM sodium phosphate buffer, 10 µL) were added and incubation was continued at 37 °C for 48 h using an Eppendorf Thermomixer at 400 rpm. To each hydrolysate internal standards of AA and AGP were added (3 µL). Afterwards, samples were ultrafiltered (Amicon Ultra, 3 kDa centrifugal filters; 13,600 × g, 30 min, 4 °C), dried by vacuum centrifugation and reconstituted to a defined volume (150 µL) by addition of H_2O for UHPLC-MS/MS analysis.

Ultra High Performance Liquid Chromatography-Mass Spectrometry (UHPLC-MS/MS)

LC-MS/MS analysis was conducted on a QTRAP 6500+ LC-MS/MS system connected to a ExionLC AD (Sciex) operated in the positive ESI mode (ion spray voltage, 5500 V): curtain gas, 35 V; temperature, 450 °C (AAs) or 500 °C (AGPs); gas 1, 55 psi; gas 2, 65 psi; collision-activated dissociation, 2 V; and entrance potential, 10 V. For compound optimization flow injection with a syringe pump (10 µL/min) and compound solutions in ACN (0.1% FA) were used.

AAs and AGPs were separated on a BEH Amide column (100 × 2.1 mm, 1.7 µm, Waters). Chromatography was performed using an injection volume of 1 µL (AAs) or 2 µL (AGPs), a flow rate of 0.4 mL/min and a column temperature of 40°C. The solvent system consisted of A: 5 mM

NH4Ac and 0.1% formic acid in water and B: 5 mM NH4Ac and 0.1% formic acid in acetonitrile/water (95/5, v/v). For AA and AGP analysis two separate methods were used sharing following gradient: 0 min, 90% B; 5 min, 85% B; 8 min, 70% B; 9 min, 0% B; 11 min, 0% B; 12 min, 90% A; 14 min, 90% B. Data acquisition and instrumental control was performed using Analyst 1.6.3 software (Sciex). AAs and AGPs were analysed in the positive multiple reaction monitoring (MRM) mode following MS/MS parameters as depicted in Table VIII.

Calibration Curve and Linear Range.

For AGP analysis stock solutions of standards were prepared in D_2O and each concentration was verified by means of quantitative NMR (qNMR). Thereafter, a mixture of analytes with concentrations of 132.5 µmol/L (**15**), 750 µmol/L (**16**), 300.5 µmol/L (**17**), 215.5 µmol/L (**18**), 214.5 µmol/L (**19**) and 118.5 µmol/L (**20**) were prepared and subsequently diluted by factors of 2, 5, 10, 20, 50, 100, 200, 500, 1000, 2000, 5000, 10000, 20000, 50000 and 100000. Afterwards, diluted analyte mixtures were mixed with constant concentrations of IS MG-H1-d_3 (**16-d_3**, 0.655 mmol/L) and imidazolysine-$^{15}N_2$ (**17**-$^{15}N_2$, 0.606 mmol/L). Triplicate UHPLC-MS/MS analysis calibration curves were prepared by plotting peak area ratios of argpyrimidine (**15**), MG-H1 (**16**), pyrraline (**18**), carboxyethyllysine (**19**) and carboxymethyllysine (**20**) to the internal standard MG-H1-d_3 (**16-**d_3) against concentration ratios of the analytes to the IS using linear regression. Calibration curve of imidazollysine (**17**) was created by plotting peak ratios to the internal standard imidazollysine-$^{15}N_2$ (**17**-$^{15}N_2$) against concentration ratios of respective analyte and internal standard.

AA analysis was conducted first by dilution (1:10, 1:20, 1:50, 1:100, 1:200, 1:500, 1:1000, 1:2000, 1:5000 and 1:10000) of an AA mix with concentrations referred to Table IX. Subsequently, to each diluted AA standard solution diluted IS (1/20 dilution of stock solution) was added to a dilution factor of 250 referred to IS concentrations in Table IX. Calibration curves were created by triplicate UHPLC-MS/MS measurements and plotting peak area ratios AAs to corresponding internal standards by using a linear regression model.

The response was linear for each analyte (AAs and AGPs) with correlation coefficients of >0.99 for chosen molar ratios and the contents of AGPs in the samples were calculated using the

respective calibration function. Determination of the limit of detection (LOD) at a signal-to-noise ratio of 3 and the limit of quantitation (LOQ) at a signal-to-noise ratio of 10 revealed the following values: LOD: ≤0.0001 µM; LOQ ≤0.0005 µM.

Nuclear Magnetic Resonance Spectroscopy (NMR)

One-dimensional ^{1}H quantitative NMR (qNMR) experiments were acquired on a 400 MHz Avance III spectrometer equipped with a Double Resonance Broadband probe (Bruker as reported by [69]. Chemical shifts are reported in parts per million, relative to solvent signal of D_2O (7.26 ppm). All pulse sequences were taken from Bruker software library. For data processing Topspin NMR software (version 3.2; Bruker) was used.

Statistical analysis

Statistical analyses were performed with Graph-Pad Prism 6 (GraphPad Software, Differences between groups were calculated by Student´s two-way unpaired t-test, two-way ANOVA or Mantel-Cox-test. Statistical significance is depicted as *P*-value (*P**<0.05; *P***<0.01; *P****<0.001; *P*****<0.00001).

Data availability

The microarray data generated from human MDSCs compared to monocytes were deposited at: https://www.ncbi.nlm.nih.gov/geo/query/acc.cgi?acc=GSE131679. The data that support the findings of this study are available from the corresponding authors upon request.

Further information can be found in the Life Sciences Reporting Summary.

References

58. Hoechst, B. *et al.* A new population of myeloid-derived suppressor cells in hepatocellular carcinoma patients induces CD4(+)CD25(+)Foxp3(+) T cells. *Gastroenterology* **135**, 234-243 (2008).

59. Weiskirchen, R. *et al.* Genetic characteristics of the human hepatic stellate cell line LX-2. *PLoS One* **8**, e75692 (2013).

60. Clausen, B.E., Burkhardt, C., Reith, W., Renkawitz, R. & Forster, I. Conditional gene targeting in macrophages and granulocytes using LysMcre mice. *Transgenic Res* **8**, 265-277 (1999).

61. Agarwal, A. *et al.* Transient Opening of the Mitochondrial Permeability Transition Pore Induces Microdomain Calcium Transients in Astrocyte Processes. *Neuron* **93**, 587-605 e587 (2017).

62. Knier, B. *et al.* Myeloid-derived suppressor cells control B cell accumulation in the central nervous system during autoimmunity. *Nat Immunol* **19**, 1341-1351 (2018).

63. Du, P., Kibbe, W.A. & Lin, S.M. lumi: a pipeline for processing Illumina microarray. *Bioinformatics (Oxford, England)* **24**, 1547-1548 (2008).

64. Smyth, G. Limma: linear models for microarray data. . In: Gentleman, R., Carey, V., Huber, W., Irizarry, R. & Dudoi, S. (eds). *In Bioinformatics and computational biology solutions using R and Bioconductor*. Springer, 2005.

65. Tripathi, S. *et al.* Meta- and Orthogonal Integration of Influenza "OMICs" Data Defines a Role for UBR4 in Virus Budding. *Cell host & microbe* **18**, 723-735 (2015).

66. Bausch-Fluck, D. *et al.* A mass spectrometric-derived cell surface protein atlas. *PLoS ONE* **10**, e0121314 (2015).

67. Ahmed, N., Argirov, O.K., Minhas, H.S., Cordeiro, C.A.A. & Thornalley, P.J. Assay of advanced glycation endproducts (AGEs): surveying AGEs by chromatographic assay with derivatization by 6-aminoquinolyl-N-hydroxysuccinimidyl-carbamate and application to Nepsilon-carboxymethyl-lysine- and Nepsilon-(1-carboxyethyl)lysine-modified albumin. *Biochem J* **364**, 1-14 (2002).

68. Salomón, T. *et al.* Ketone Body Acetoacetate Buffers Methylglyoxal via a Non-enzymatic Conversion during Diabetic and Dietary Ketosis. *Cell Chemical Biology* **24**, 935-943.e937 (2017).

69. Frank, O., Kreissl, J.K., Daschner, A. & Hofmann, T. Accurate determination of reference materials and natural isolates by means of quantitative (1)h NMR spectroscopy. *J Agric Food Chem* **62**, 2506-2515 (2014).

Figure 1

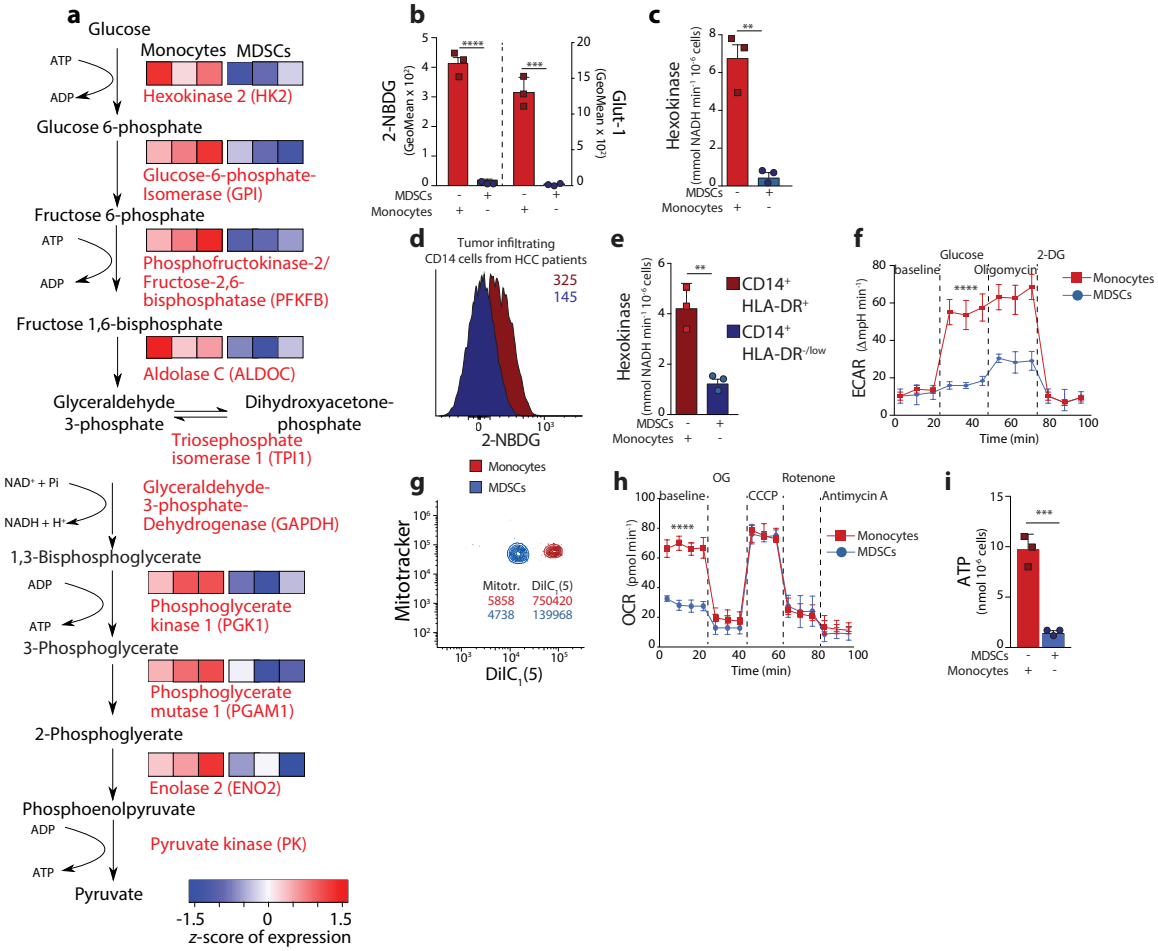
a
Glucose
Monocytes MDSCs
ATP
ADP
Hexokinase 2 (HK2)
Glucose 6-phosphate
Glucose-6-phosphate-Isomerase (GPI)
Fructose 6-phosphate
Phosphofructokinase-2/Fructose-2,6-bisphosphatase (PFKFB)
Fructose 1,6-bisphosphate
Aldolase C (ALDOC)
Glyceraldehyde 3-phosphate
Dihydroxyacetone-phosphate
Triosephosphate isomerase 1 (TPI1)
NAD+ + Pi
NADH + H+
Glyceraldehyde-3-phosphate-Dehydrogenase (GAPDH)
1,3-Bisphosphoglycerate
Phosphoglycerate kinase 1 (PGK1)
3-Phosphoglycerate
Phosphoglycerate mutase 1 (PGAM1)
2-Phosphoglyerate
Enolase 2 (ENO2)
Phosphoenolpyruvate
Pyruvate kinase (PK)
Pyruvate
-1.5 0 1.5
z-score of expression
b
2-NBDG (GeoMean x 10²)
Glut-1 (GeoMean x 10²)
MDSCs
Monocytes
c
Hexokinase (mmol NADH min⁻¹ 10⁻⁶ cells)
d
Tumor infiltrating CD14 cells from HCC patients
325
145
2-NBDG
e
CD14⁺ HLA-DR⁺
CD14⁺ HLA-DR⁻/low
f
Glucose
2-DG
baseline
Oligomycin
ECAR (ΔmpH min⁻¹)
Monocytes
MDSCs
Time (min)
g
Monocytes
MDSCs
Mitotracker
Mitotr. DilC1(5)
5858 750420
4738 139968
DilC1(5)
h
OG
Rotenone
baseline
CCCP
Antimycin A
OCR (pmol min⁻¹)
Time (min)
i
ATP (nmol 10⁻⁶ cells)

Figure 2

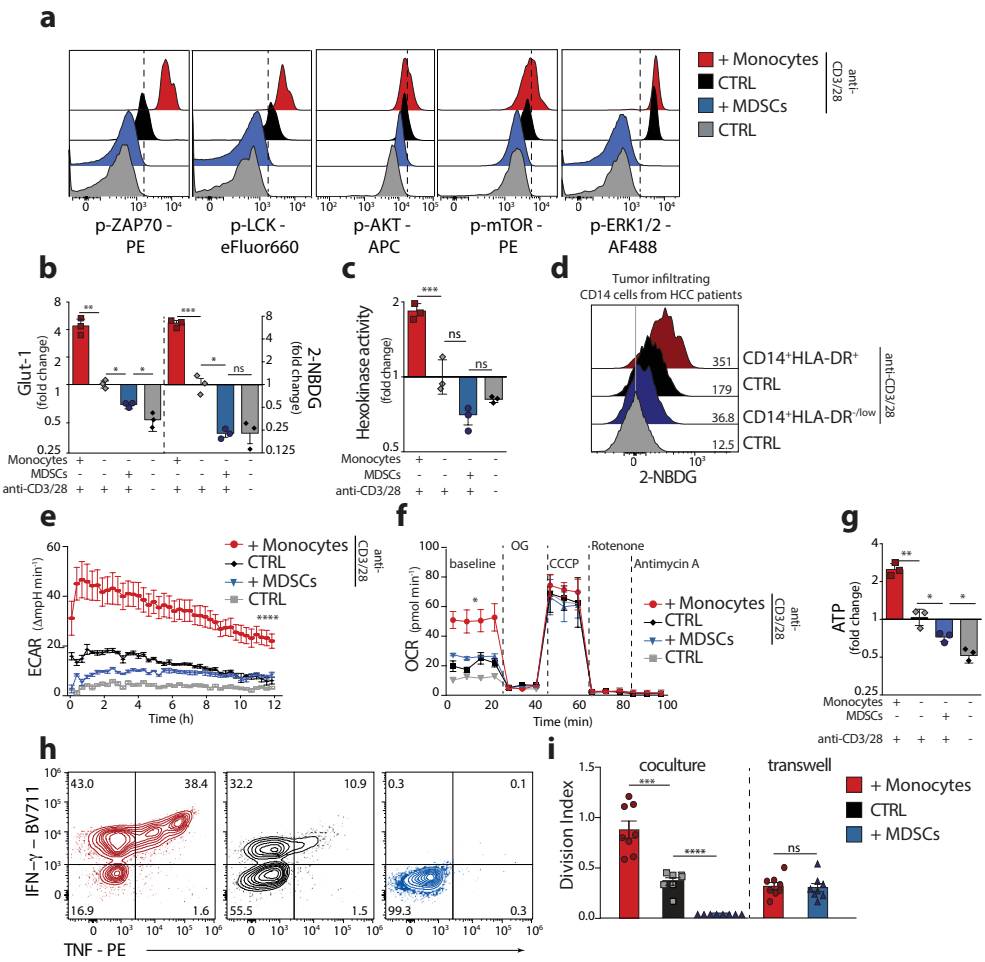
a
+ Monocytes
CTRL
+ MDSCs
CTRL
anti-CD3/28
p-ZAP70 - PE
p-LCK - eFluor660
p-AKT - APC
p-mTOR - PE
p-ERK1/2 - AF488
b
Glut-1 (fold change)
2-NBDG (fold change)
Monocytes
MDSCs
anti-CD3/28
c
Hexokinase activity (fold change)
ns
d
Tumor infiltrating CD14 cells from HCC patients
351
CD14+HLA-DR+
179
CTRL
36.8
CD14+HLA-DR-/low
12.5
CTRL
anti-CD3/28
2-NBDG
e
+ Monocytes
CTRL
+ MDSCs
CTRL
anti-CD3/28
ECAR (ΔmpH min-1)
Time (h)
f
baseline
OG
CCCP
Rotenone
Antimycin A
OCR (pmol min-1)
Time (min)
g
ATP (fold change)
h
43.0
38.4
16.9
1.6
32.2
10.9
55.5
1.5
0.3
0.1
99.3
0.3
IFN-γ – BV711
TNF - PE
i
coculture
transwell
Division Index
+ Monocytes
CTRL
+ MDSCs

Figure 3

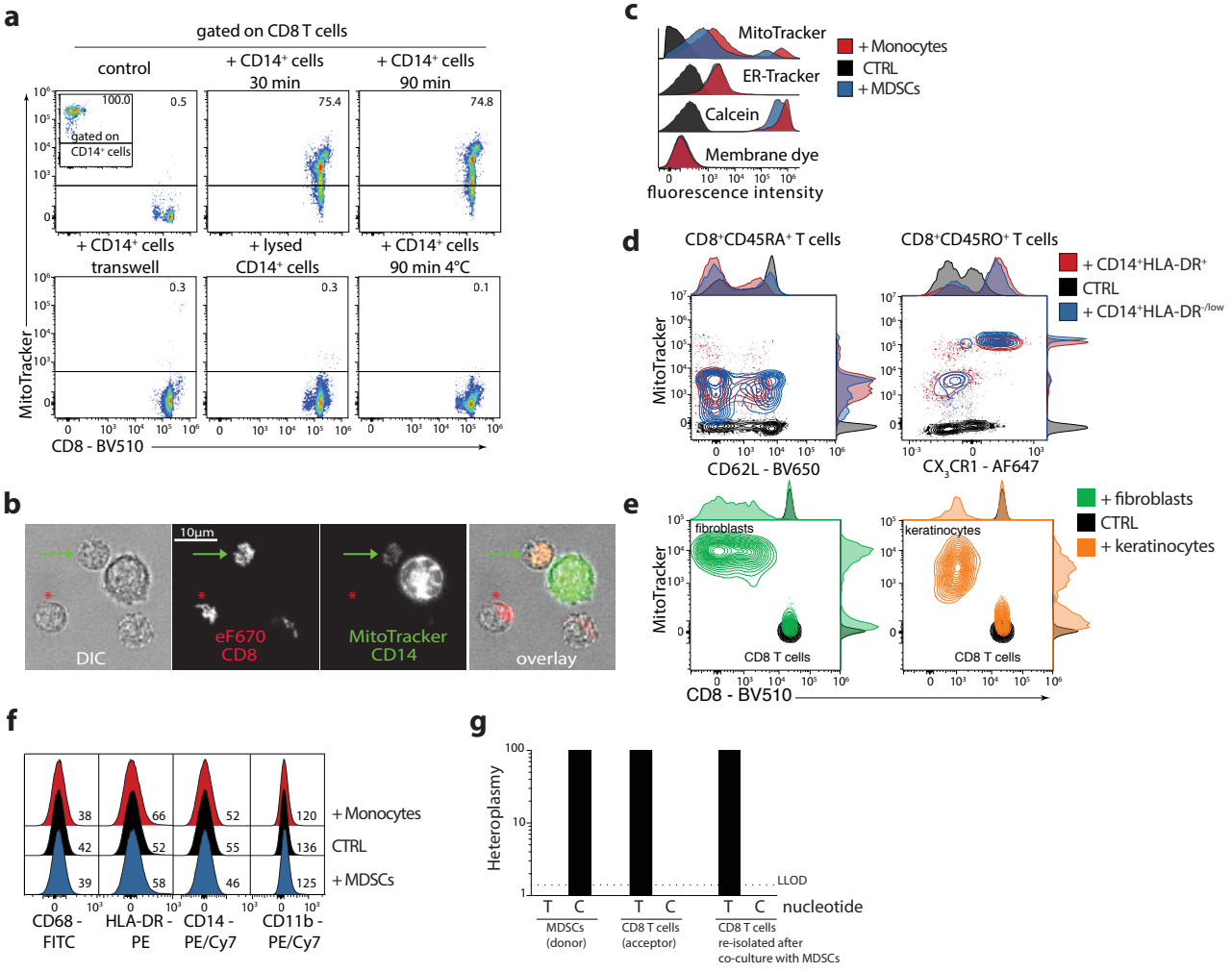
a
gated on CD8 T cells
control
+ CD14+ cells 30 min
+ CD14+ cells 90 min
100.0
0.5
gated on CD14+ cells
75.4
74.8
+ CD14+ cells transwell
+ lysed CD14+ cells
+ CD14+ cells 90 min 4°C
0.3
0.3
0.1
MitoTracker
CD8 - BV510
b
10µm
DIC
eF670 CD8
MitoTracker CD14
overlay
c
MitoTracker
ER-Tracker
Calcein
Membrane dye
fluorescence intensity
+ Monocytes
CTRL
+ MDSCs
d
CD8+CD45RA+ T cells
CD8+CD45RO+ T cells
+ CD14+HLA-DR+
CTRL
+ CD14+HLA-DR-/low
MitoTracker
CD62L - BV650
CX3CR1 - AF647
e
+ fibroblasts
CTRL
+ keratinocytes
fibroblasts
keratinocytes
CD8 T cells
MitoTracker
CD8 - BV510
f
38
66
52
120
42
52
55
136
39
58
46
125
+ Monocytes
CTRL
+ MDSCs
CD68 - FITC
HLA-DR - PE
CD14 - PE/Cy7
CD11b - PE/Cy7
g
Heteroplasmy
100
10
1
LLOD
T C
T C
T C
nucleotide
MDSCs (donor)
CD8 T cells (acceptor)
CD8 T cells re-isolated after co-culture with MDSCs

Figure 4

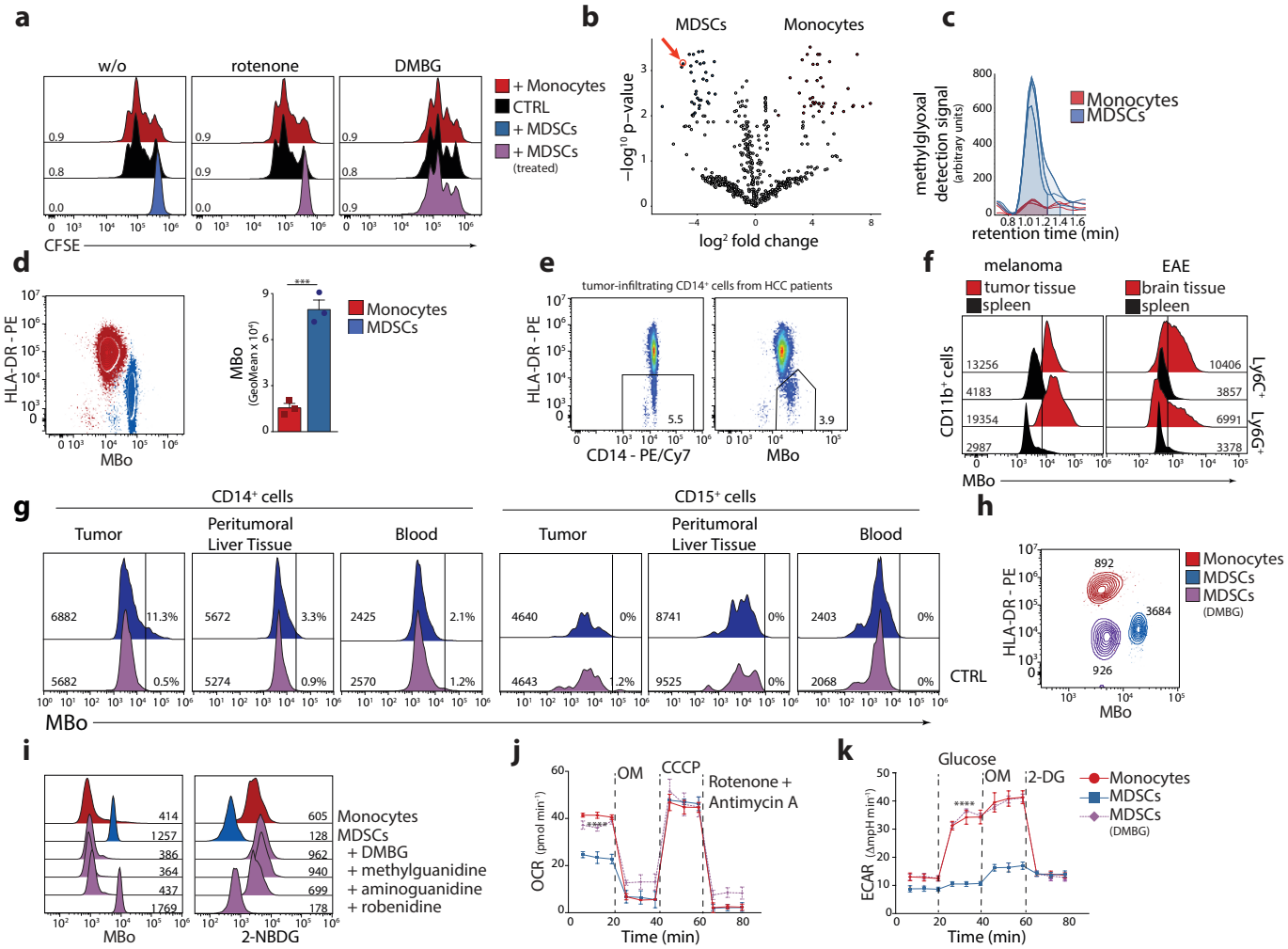
a
w/o
rotenone
DMBG
+ Monocytes
CTRL
+ MDSCs
+ MDSCs (treated)
CFSE
b
MDSCs
Monocytes
−log10 p-value
log2 fold change
c
methylglyoxal detection signal (arbitrary units)
Monocytes
MDSCs
retention time (min)
d
HLA-DR - PE
MBo
MBo (GeoMean x 10³)
Monocytes
MDSCs
e
tumor-infiltrating CD14+ cells from HCC patients
HLA-DR - PE
CD14 - PE/Cy7
MBo
f
melanoma
tumor tissue
spleen
EAE
brain tissue
spleen
CD11b+ cells
Ly6C+
Ly6G+
MBo
g
CD14+ cells
CD15+ cells
Tumor
Peritumoral Liver Tissue
Blood
CTRL
MBo
h
HLA-DR - PE
MBo
Monocytes
MDSCs
MDSCs (DMBG)
i
Monocytes
MDSCs
+ DMBG
+ methylguanidine
+ aminoguanidine
+ robenidine
MBo
2-NBDG
j
OM
CCCP
Rotenone + Antimycin A
OCR (pmol min⁻¹)
Time (min)
k
Glucose
OM
2-DG
Monocytes
MDSCs
MDSCs (DMBG)
ECAR (ΔmpH min⁻¹)
Time (min)

Figure 5

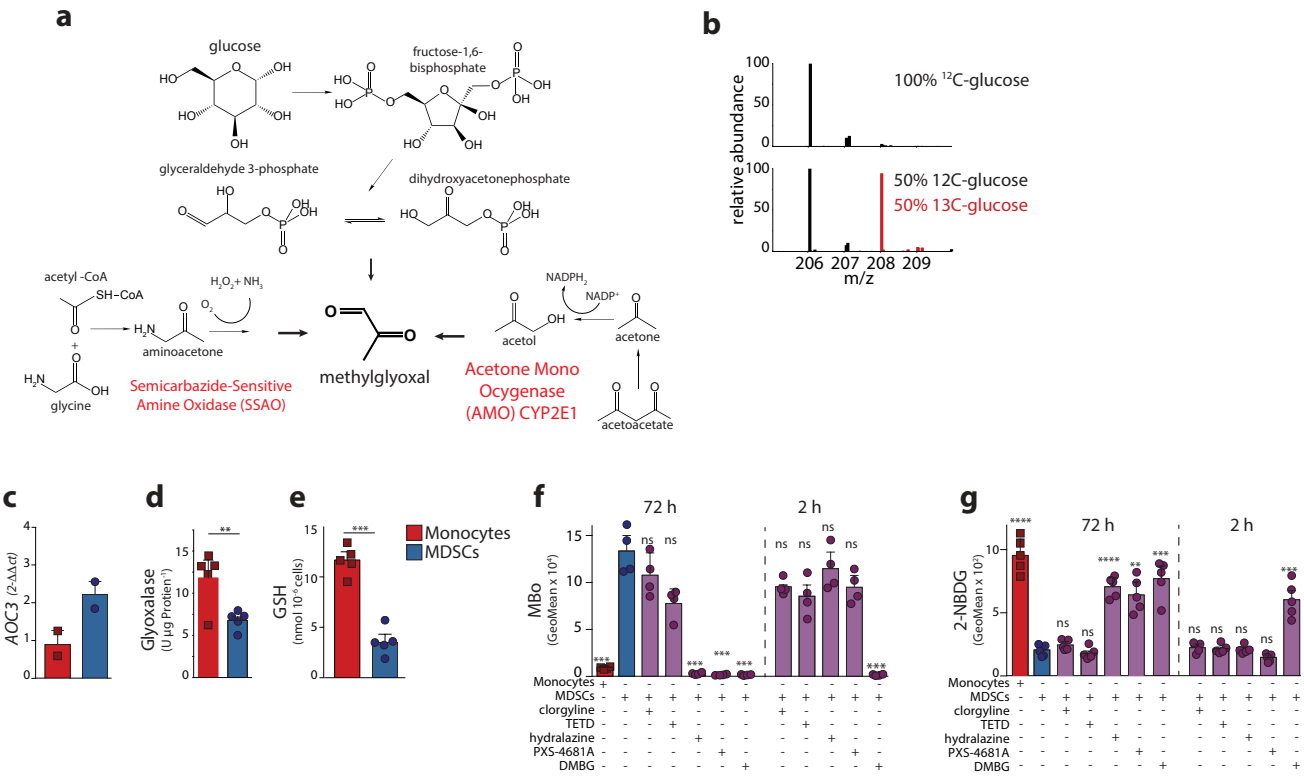
a
glucose
fructose-1,6-bisphosphate
glyceraldehyde 3-phosphate
dihydroxyacetonephosphate
acetyl -CoA
SH–CoA
aminoacetone
glycine
Semicarbazide-Sensitive Amine Oxidase (SSAO)
methylglyoxal
acetol
acetone
acetoacetate
Acetone Mono Ocygenase (AMO) CYP2E1
b
relative abundance
100% 12C-glucose
50% 12C-glucose
50% 13C-glucose
206 207 208 209
m/z
c
AOC3 (2-ΔΔct)
d
Glyoxalase (U µg Protien-1)
e
GSH (nmol 10-6 cells)
Monocytes
MDSCs
f
72 h
2 h
MBo (GeoMean x 10³)
Monocytes
MDSCs
clorgyline
TETD
hydralazine
PXS-4681A
DMBG
g
72 h
2 h
2-NBDG (GeoMean x 10³)
Monocytes
MDSCs
clorgyline
TETD
hydralazine
PXS-4681A
DMBG

Figure 6

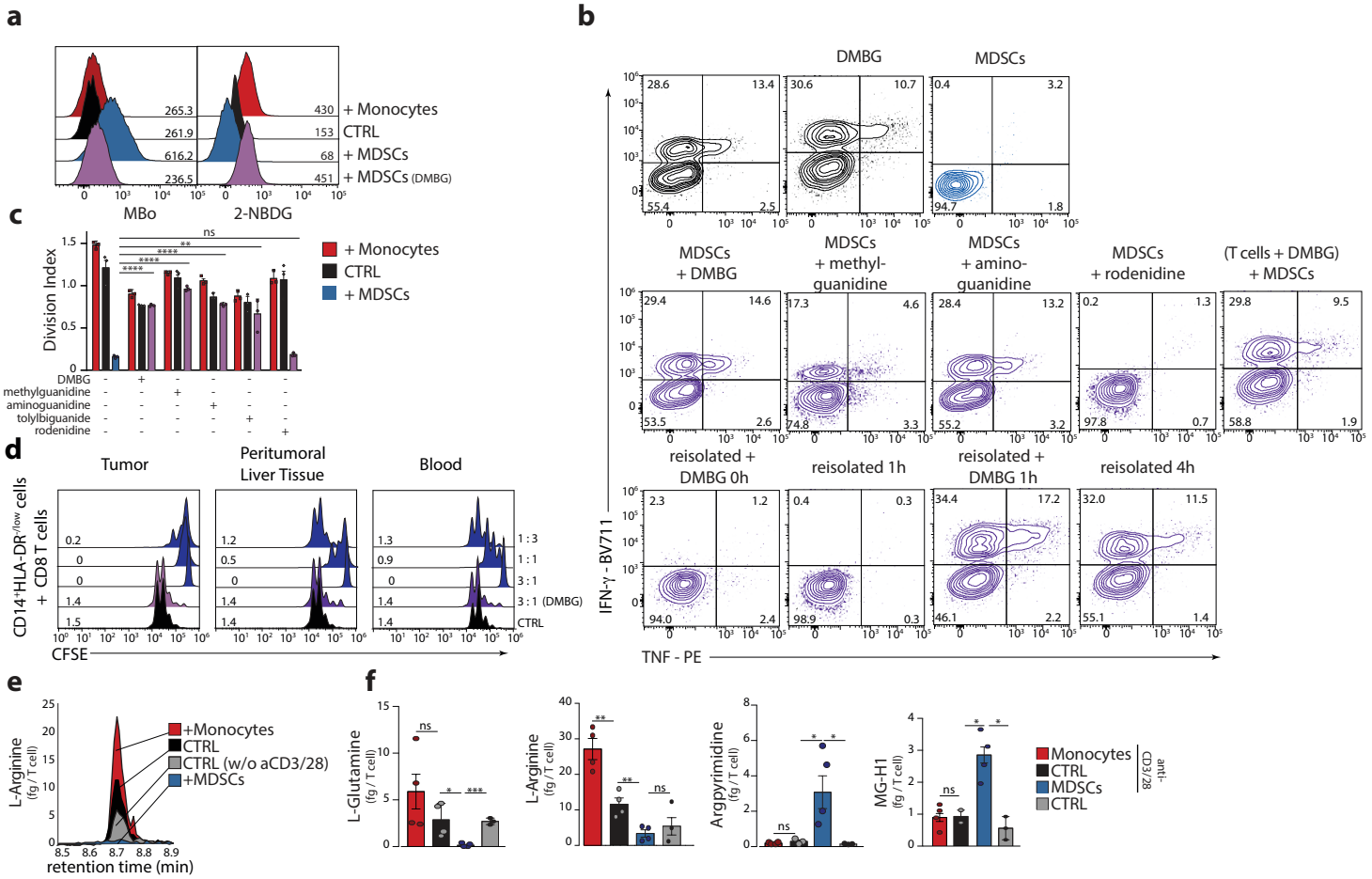
a
265.3
261.9
616.2
236.5
430
153
68
451
+ Monocytes
CTRL
+ MDSCs
+ MDSCs (DMBG)
MBo
2-NBDG
c
Division Index
+ Monocytes
CTRL
+ MDSCs
DMBG
methylguanidine
aminoguanidine
tolylbiguanide
rodenidine
b
DMBG
MDSCs
MDSCs + DMBG
MDSCs + methyl-guanidine
MDSCs + amino-guanidine
MDSCs + rodenidine
(T cells + DMBG) + MDSCs
reisolated + DMBG 0h
reisolated 1h
reisolated + DMBG 1h
reisolated 4h
IFN-γ - BV711
TNF - PE
d
Tumor
Peritumoral Liver Tissue
Blood
CD14+HLA-DR-/low cells + CD8 T cells
CFSE
1 : 3
1 : 1
3 : 1
3 : 1 (DMBG)
CTRL
e
L-Arginine (fg / T cell)
+Monocytes
CTRL
CTRL (w/o aCD3/28)
+MDSCs
retention time (min)
f
L-Glutamine (fg / T cell)
L-Arginine (fg / T cell)
Argpyrimidine (fg / T cell)
MG-H1 (fg / T cell)
Monocytes
CTRL
MDSCs
CTRL
anti-CD3/28

Figure 7

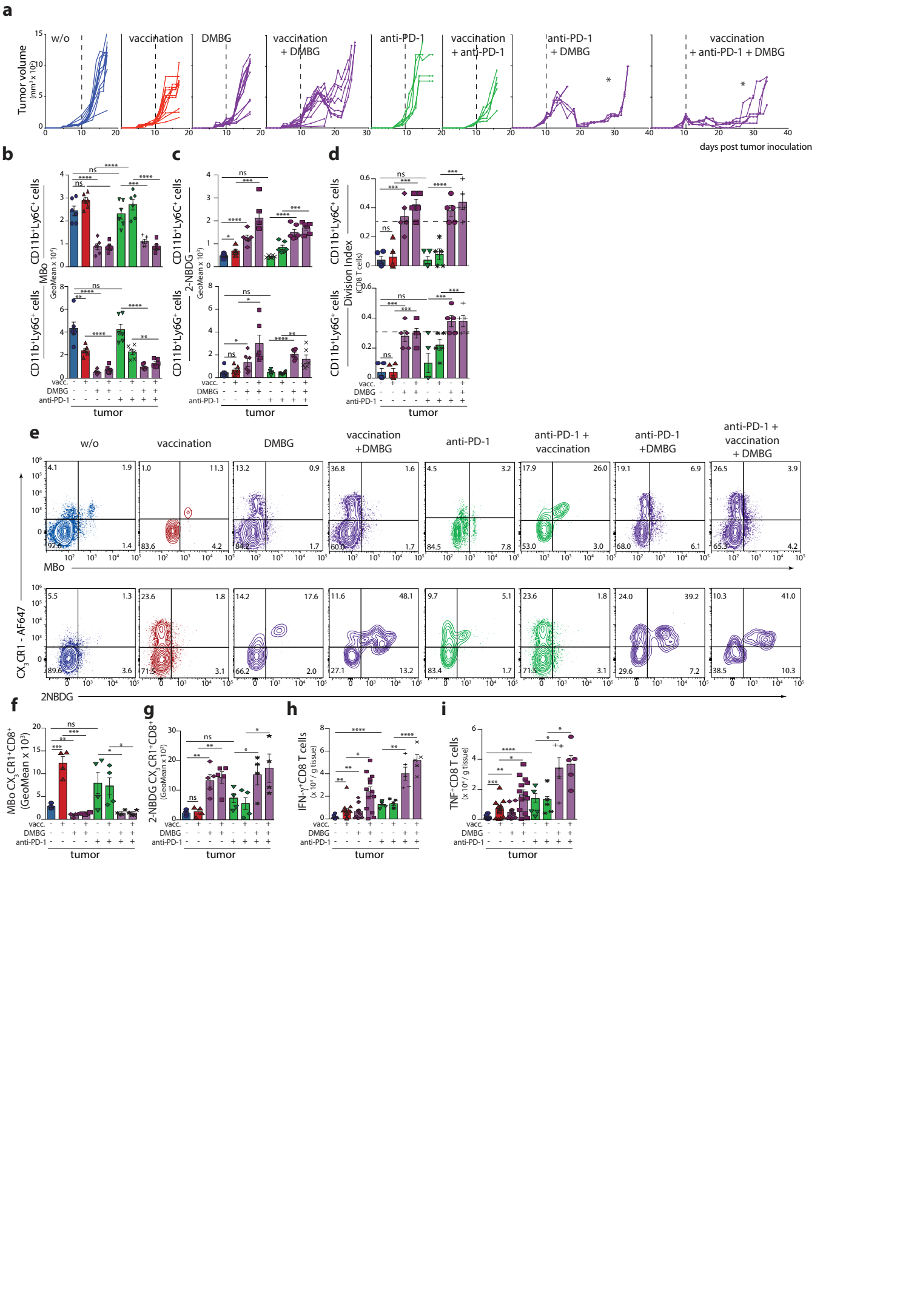
a
w/o
vaccination
DMBG
vaccination + DMBG
anti-PD-1
vaccination + anti-PD-1
anti-PD-1 + DMBG
vaccination + anti-PD-1 + DMBG
Tumor volume (mm³ x 10²)
days post tumor inoculation
b
c
d
CD11b⁺Ly6C⁺ cells
CD11b⁺Ly6G⁺ cells
MBo GeoMean x 10³
2-NBDG GeoMean x 10³
Division Index (CD8 T cells)
vacc.
DMBG
anti-PD-1
tumor
e
w/o
vaccination
DMBG
vaccination +DMBG
anti-PD-1
anti-PD-1 + vaccination
anti-PD-1 +DMBG
anti-PD-1 + vaccination + DMBG
MBo
CX3CR1 - AF647
2NBDG
f
g
h
i
MBo CX3CR1⁺CD8⁺ (GeoMean x 10³)
2-NBDG CX3CR1⁺CD8⁺ (GeoMean x 10³)
IFN-γ⁺CD8 T cells (x 10⁴ / g tissue)
TNF⁺CD8 T cells (x 10⁴ / g tissue)